Mon. Not. R. Astron. Soc. **383,** 1519–1537 (2008) doi:10.1111/j.1365-2966.2007.12664.x

The Arecibo Galaxy Environment Survey – II. A H I view of the Abell cluster 1367 and its outskirts

L. Cortese,[1⋆] R. F. Minchin,[2] R. R. Auld,[1] J. I. Davies,[1] B. Catinella,[2,3] E. Momjian,[2,13] J. L. Rosenberg,[4] R. Taylor,[1] G. Gavazzi,[5] K. O'Neil,[6] M. Baes,[7] A. Boselli,[8] G. Bothun,[9] B. Koribalski,[10] S. Schneider[11] and W. van Driel[12]

[1]*School of Physics and Astronomy, Cardiff University, Cardiff CF24 3AA*
[2]*NAIC-Arecibo Observatory, HC3 Box 53995, Arecibo, PR 00612, USA*
[3]*Max-Planck-Institut für Astrophysik, D-85748 Garching, Germany*
[4]*Harvard-Smithsonian Center for Astrophysics, 60 Garden Street, MS 65, Cambridge, MA 02138-1516, USA*
[5]*Universitá degli Studi di Milano-Bicocca, Piazza della Scienza 3, 20126 Milano, Italy*
[6]*National Radio Astronomy Observatory, Green Bank, WV 24944, USA*
[7]*Sterrenkundig Observatorium, Universiteit Gent, Krijgslaan 281 S9, B-900 Gent, Belgium*
[8]*Laboratoire d'Astrophysique de Marseille, BP8, Traverse du Siphon, F-13376 Marseille, France*
[9]*Physics Department, University of Oregon, 1371 East 13th Avenue, Eugene, OR 97403, USA*
[10]*Australia Telescope National Facility, CSIRO, Epping, NSW, Australia*
[11]*Department of Astronomy, University of Massachusetts, Amherst, MA 01003, USA*
[12]*Observatoire de Meudon, 5 Place Jules Janssen, 92195 Meudon, France*
[13]*NRAO, P.O. Box O, Socorro, NM 87801, USA*

Accepted 2007 October 28. Received 2007 October 1; in original form 2007 August 10

ABSTRACT

We present 21 cm H I line observations of 5×1 deg^2 centred on the local Abell cluster 1367 obtained as part of the Arecibo Galaxy Environment Survey. One hundred sources are detected (79 new H I measurements and 50 new redshifts), more than half belonging to the cluster core and its infalling region. Combining the H I data with Sloan Digital Sky Survey (SDSS) optical imaging, we show that our H I selected sample follows scaling relations similar to the ones usually observed in optically selected samples. Interestingly, all galaxies in our sample appear to have nearly the same baryon fraction independently of their size, surface brightness and luminosity. The most striking difference between H I and optically selected samples resides in their large-scale distribution: whereas optical and X-ray observations trace the cluster core very well, in H I there is almost no evidence of the presence of the cluster. Some implications on the determination of the cluster luminosity function and H I distribution for samples selected at different wavelength are also discussed.

Key words: surveys – galaxies: clusters: individual: A1367 – galaxies: evolution – galaxies: peculiar – radio lines: galaxies.

1 INTRODUCTION

With the advent of wide field surveys, our knowledge of galaxy properties has significantly improved. The large amount of high-quality data of nearby and high-redshift objects obtained so far are allowing astronomers to shed light on how galaxies formed and evolved at different redshifts and in different environments (e.g. Cowie et al. 1996; Gavazzi, Pierini & Boselli 1996; Kauffmann et al. 2003). However, our picture of the Universe still remains limited since it is mostly based on the study of rest-frame optical-selected objects. First of all, optically selected galaxies already contain, by definition, a large amount of stars which may not be the case in younger or less evolved galaxies. Secondly, surface brightness selection is very dramatic, and nearly all catalogued objects lie in an extremely narrow range of surface brightnesses (Freeman 1970).

Since each wavelength has its own selection effects and traces different baryonic components, the combination of blind surveys at various frequencies is of vital importance. Alternative methods of baryon selection will allow us to have a less biased view of our Universe and enable us to correctly reconstruct the evolutionary history of galaxies (e.g. Buat et al. 2007). In particular, the most interesting results can come from the comparison of optical surveys with blind surveys tracing components not directly related to stellar emission like, for example, neutral and molecular hydrogen. For molecular hydrogen, we will have to wait a couple of years for the first

⋆E-mail: luca.cortese@astro.cf.ac.uk

results from Atacama Large Millimeter Array, but with the advent of multibeam instruments on large single dish radio telescopes it has become possible during the last decade to carry out fully sampled blind H I surveys of the sky (e.g. Henning et al. 2000; Rosenberg & Schneider 2000; Barnes et al. 2001; Lang et al. 2003; Minchin et al. 2003; Davies et al. 2004). Neutral hydrogen is extremely important because it represents the fuel for the future star formation activity of a galaxy. It is also one of the galactic components that can most easily be affected by environmental mechanism (e.g. ram pressure, tidal interaction) influencing its star formation history. Therefore, H I line observations of galaxies can provide us with some of the most powerful diagnostics on the role of the environment in regulating the evolution of galaxies (Haynes & Giovanelli 1984; Giovanelli & Haynes 1985). What we lack is deep and high spatial resolution H I blind surveys of cluster of galaxies and their outskirts. The H I Parkes All-Sky Survey (HIPASS) has represented a real breakthrough for H I blind surveys, but its low spatial resolution ($\sim$15 arcmin) has made it very difficult to carry out detailed studies of high-density regions. Fortunately, with the refurbishing of the 305-m Arecibo radio telescope, blind H I surveys with much improved sensitivity, spatial (3.5 arcmin beam^{-1}) and velocity (5 km s^{-1}) resolution have become possible thanks to the installation of the ALFA multibeam instrument.

The Abell cluster 1367, due to its proximity ($z \sim 0.0216, V \sim 6500\,\mathrm{km\,s^{-1}}$) and to the fact that it is currently forming at the intersection of two filaments in the Great Wall (Cortese et al. 2004), represents an ideal target for H I surveys (e.g. Sullivan et al. 1981; Chincarini, Giovanelli & Haynes 1983; Gavazzi 1987; Solanes et al. 2001; Gavazzi et al. 2006). It is ideal for the study of the properties of H I selected galaxies and environmental effects. For these reasons, Abell 1367 is one of the region observed as a part of the Arecibo Galaxy Environment Survey (AGES; Auld et al. 2006), one of the new H I blind survey carried out with the ALFA multibeam system.[1] AGES aims to study the atomic hydrogen properties of different galactic environments to faint sensitivity limits; low H I masses ($6 \times 10^8\,\mathrm{M_\odot}$, assuming a 200 km s^{-1} velocity width at 92.8 Mpc, the distance of the A1367 cluster) and column densities of $\sim 3 \times 10^{18}$ cm^2 (for a source that fills the beam). The environments AGES will survey range from apparent voids in the large-scale structure of galaxies, via isolated spiral galaxies and their haloes, to galaxy-rich regions associated with galaxy clusters and filamentary structures. AGES plans to cover 5×4 deg^2 centred on Abell 1367. Here, we report on the early results obtained from observations of a subset of the whole AGES-A1367 region: a 5×1 deg^2 area centred on the cluster core.

2 AGES OBSERVATIONS AND DATA REDUCTION

As part of the AGES, we observed the Abell 1367 region in 2006 May and 2007 April using the ALFA feed array at the 305-m Arecibo Telescope. A total of $\sim$63 h observing time was allocated with an average observing time of $\sim$2.3 h per night. Since the allocated time was insufficient to cover all the AGES-A1367 region (5×4 deg^2), we decided to give the highest priority to the cluster centre and its immediate outskirts covering a strip of $\sim 5 \times 1$ deg^2 [11:34:00 < RA(J.2000) < 11:54:15, 19:15 < Dec.(J.2000) < 20:20] centred on the cluster core. The observation and data reduction techniques adopted by AGES are extensively described in Auld et al. (2006); here, we will only provide a brief summary of them.

AGES uses the seven-feed ALFA multibeam receiver and a spectral line backend capable of instantaneously recording spectra from the two linear polarizations of each beam and covering a bandwidth of 100 MHz. The angular resolution is given by the size of the ALFA beams ($\sim 3.3 \times 3.8$ arcmin^2) and the velocity resolution is $\sim$25 kHz, corresponding to $\sim$5.5 km s^{-1}. Observations are performed in *drift scan mode* (e.g. Giovanelli et al. 2005): the array is kept at a fixed azimuth and elevation while the sky drifts overhead. The Earth's rotation rate governs the on-source time in a drift scan. For Arecibo, this means that each point in the sky takes $\sim$12 s to cross the beam. 25 separate scans are then required to reach the 300 s beam^{-1} integration time. In order to compensate for the change in parallactic angle, and thus achieve uniform sky coverage, ALFA must be rotated before every scan and, in order to attain fully sampled sky coverage, it is necessary to stagger the declination (Dec.) of individual scans by $\sim$1 arcmin (half the beam separation). We record data every second and total power values for each of the seven beams, both polarizations and 4096 channels, are recorded as four-bit floating point numbers. Calibration is performed at the beginning of every scan using a high-temperature noise diode that is injected into each beam for a duration of 1 s. A uniform final depth of $\sim$300 s was achieved for all of the area observed.

Data reduction was performed using the AIPS++ packages LIVEDATA and GRIDZILLA (Barnes et al. 2001), developed by the Australian Telescope National Facility (ATNF). LIVEDATA performs bandpass estimation and removal, Doppler tracking, and calibrates the residual spectrum. GRIDZILLA is a gridding package that co-adds all the spectra using a suitable algorithm, to produce 3D data cubes. The Abell 1367 5×1 deg^2 region was gridded using a median gridding technique into 1×1 deg^2 pixels, each of which contains a 4096 channel spectrum, and was smoothed at a velocity resolution of 10 km s^{-1}. The AGES observing strategy is highly successful at reducing sidelobe variations by making a Nyquist-sampled map with every ALFA beam individually. Thus, when the observations are median combined, the variations across the beams are removed, leaving a circular beam with symmetrical sidelobes at a $\sim$5–10 per cent level (Minchin et al. 2007). The output data cube has two spatial dimensions, and the spectral dimension can be chosen by the user to be frequency, wavelength or velocity. The noise distribution is fairly Gaussian with a standard deviation of 0.8439 ± 0.0003 mJy, consistent with the expected value (Auld et al. 2006) for minimal smoothing of the beam. The cube is publicly available and can be downloaded at the following link http://www.naic.edu//ages/public_data.html.

2.1 Data contamination: radio frequency interference, the Milky Way and 3C264

Radio frequency interference (RFI) represents a constant source of contamination in certain regions of the observed spectral window. In particular, two main RFI sources were present in all the scans: the San Juan Federal Aviation Administration radar at 1350 MHz and its third harmonic at 1387.8 MHz. In addition, an intermittent source of RFI (Global Positioning System (GPS) satellite L3) appeared only in some of the scans at approximately 1381 MHz. The strong constant sources at 1350 MHz ($V \sim 14620 \pm 140\,\mathrm{km\,s^{-1}}$) and 1387.8 MHz ($V \sim 7009 \pm 19\,\mathrm{km\,s^{-1}}$) completely obscure a part of the cosmic volume: in particular, the 1387.8 MHz RFI lies approximately at the velocity of Abell 1367 making part of the

[1] The other three main extragalactic ALFA surveys are The Arecibo Legacy Fast ALFA Survey (ALFALFA) (Giovanelli et al. 2005), ALFA Ultra-deep Survey (Freudling et al. 2005) and Zone of Avoidance Survey (Henning et al. 2006).

cluster volume inaccessible. The intermittent GPS source at 1381 MHz ($V \sim 8500\,\mathrm{km\,s^{-1}}$) reduces our sensitivity limit and could significantly influence the number of sources detected in a frequency range $\sim$300 $\mathrm{km\,s^{-1}}$ wide.

In addition to the RFI, another two sources of contamination affect our data. The first one is the Galaxy: LIVEDATA is not able to correctly subtract the strong emission from the Milky Way, resulting in a blindness of our survey in about the velocity range $-50 < V < +50\,\mathrm{km\,s^{-1}}$. Moreover, the Abell 1367 region includes the 3C264 radio galaxy (RA = 11:45:05.5, Dec. = +19:36:23). This strong radio source has a 1.4 GHz continuum flux of $\sim$5 Jy, producing strong spectral standing waves and making an $\sim$4 arcmin radius region around the galaxy inaccessible.

2.2 Source extraction

In every blind survey, a crucial step in the data reduction is represented by the source extraction. The objective is to obtain a catalogue of confirmed sources to well-defined selection limits: as the signal-to-noise ratio (S/N) decreases, the contamination by spurious noise signals quickly rises. Detection techniques need to be optimised to discriminate real from spurious signals as well as possible.

Currently, source extraction is carried out using three different methods: the cube is visually inspected independently by two of us (in this case RRA and LC) and by an automatic extractor (Polyfind, written by R. F. Minchin) based on a peak flux threshold. The automatic extractor is essentially based on the cross-correlation with templates method described by Davies et al. (2001). The program initially looks for peak values above a pre-defined value (in this case 4σ) and then cross-correlates with templates accepting the best fit as long as the correlation coefficient is above 0.75 and the total S/N of the detection is above 4 (Davies et al. 2004). Automatically extracted candidates are then checked 'by eye', visually inspecting the full AGES spectrum summed from a $5 \times 5\,\mathrm{arcmin^2}$ box around the position of the detection. The aim of this process is to quickly remove obvious spurious detections while not rejecting any real source. These methods provided a list of 104 candidate H I sources,[2] of which 78 were detected by all the three different signal extraction techniques. In the following, we will refer to these 78 objects as 'sure' sources and to the remaining 26 as 'possible' sources.

The distribution of the total 21 cm flux as a function of the line width at the 50 per cent level of peak maximum for our 104 candidate sources is shown in Fig. 1. Filled circles indicate 'sure' sources while empty circles are 'possible' sources. The void in the bottom right part of the plot (i.e. large velocity widths and small fluxes) is due to a selection effect present in the source extraction technique: at fixed low total flux, it is easier to detect a narrow H I source, since the survey is not flux but surface brightness limited. In order to compare the AGES S/N threshold with the recent results presented by ALFALFA (Giovanelli et al. 2007), we plotted in Fig. 1 a S/N limit of $\mathrm{S/N_{tot}} = 6.5$ for our survey, where (Saintonge 2007)

$$\mathrm{S/N_{tot}} = \frac{1000 \times F_{\mathrm{tot}}}{W_{50}} \times \frac{w^{1/2}}{\mathrm{rms}}, \quad (1)$$

F_{tot} is the total flux in $\mathrm{Jy\,km\,s^{-1}}$, W_{50} is the velocity width measured at the 50 per cent level, w is either $W_{50}/(2 \times \Delta V)$ for $W_{50} < 400\,\mathrm{km\,s^{-1}}$ or $400/(2 \times \Delta V)$ for $W_{50} \geqslant 400\,\mathrm{km\,s^{-1}}$, ΔV is the spectral velocity resolution and *rms* is the root mean square noise across the spectrum measured in mJy at *res.* spectral resolution. In our case, *res.* = 10 $\mathrm{km\,s^{-1}}$. The great majority of our 'sure' sources lie well above $\mathrm{S/N_{tot}} = 6.5$ while the 'possible' sources have $\mathrm{S/N_{tot}} \approx 6.5$, in agreement with Saintonge (2007). This also suggests that for our sample $\mathrm{S/N_{tot}} = 6.5$ is a reliable threshold for discriminating between 'sure' and 'possible' sources.

[2] Here, we do not include two extended high-velocity cloud (HVC) complexes extending over a great part of the observed region at $140 < V < 210\,\mathrm{km\,s^{-1}}$. These systems are described in the Appendix.

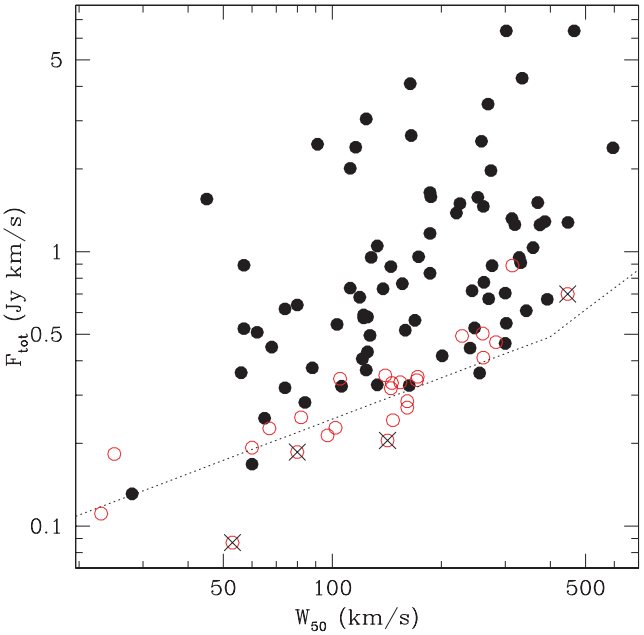

Figure 1. The distribution of the 104 H I source candidates detected in the AGES-A1367 cube. Filled circles indicate 'sure' sources (i.e. detected by all the three extraction methods adopted) and empty circles are sources not detected by all the three extraction methods and investigated with follow-up L-wide observations (see Section 3). Crosses indicate those sources that have not been confirmed by follow-up observations. The dotted line shows the ALFALFA reliability limit, $\mathrm{S/N_{tot}} = 6.5$ (Saintonge 2007).

3 L-WIDE RADIO FOLLOW-UP OBSERVATIONS

In order to test the reliability of our extraction technique and the real nature of the 26 'possible' sources, 10 h of telescope time was scheduled with the Arecibo single pixel L-band wide (LBW) receiver in 2007 April. The LBW observations were made covering a spectral band of 12.5 MHz (2048 spectral channels) centred at the expected source recessional velocity. The integration time varied between 5 and 10 min depending on the intensity of the source, reaching an rms in the range $\sim$0.5–0.8 mJy $\mathrm{beam^{-1}}$ at a velocity resolution of 10 $\mathrm{km\,s^{-1}}$. All observations were taken using the position-switching technique, with each blank sky (or OFF) position observed for the same duration, and over the same portion of the telescope dish (Az and El) as the on-source (ON) observation. Each 5 min + 5 min ON + OFF pair was followed by a 10 s ON + OFF observation of a calibrated noise diode. None of the 26 observed sources lies within the sidelobes of a 'sure' H I detection, making unlikely a sidelobe contamination of the L-wide follow-up observations. Of the 26 'possible' sources, only four (indicated with crosses in Fig. 1) were not confirmed by Arecibo follow-up observations. We therefore have a sample of 100 sure H I sources detected in the $5 \times 1\,\mathrm{deg^2}$ observed by AGES in the Abell 1367 region.

4 SOURCE CATALOGUES

All the 100 sources in the sample were inspected and parametrized using the MIRIAD task MBSPECT (Sault et al. 1995). The source position was estimated from a Gaussian fit to the moment map within the galaxy velocity range, and the spectrum was then extracted from the data cubes. This spectrum is a weighted average, with the weight depending on the distance of each pixel from the fitted position. Velocity widths were then measured at the 20 and 50 per cent levels (W_{20} and W_{50}) relative to the peak signal, using a width-maximizing algorithm (Lewis 1983). The uncertainties in each derived quantity are computed following the recipes given by Koribalski et al. (2004). In Table 1, we present the main parameters of all the 100 H I sources detected in the cube, namely, Col. 1: H I source ID. Cols 2–3: H I RA (J2000) coordinate and relative error. Cols 4–5: H I Dec. (J2000) coordinate and relative error. Col. 6: heliocentric velocity and relative error (*cz*, i.e. optical reference frame), measured as the mid-point between the velocities where the flux density reaches 50 per cent of peak maximum level. Col. 7: velocity width and relative error of the source line profile measured at the 50 per cent level of peak maximum. The velocity widths are not corrected for instrumental broadening, turbulent motions, disc inclination or cosmological effects. Col. 8: velocity width and relative error of the source line profile measured at the 20 per cent level. Col. 9: peak flux density and relative error in mJy. Col. 10: total flux and relative error in Jy km s^{-1}. Col. 11: object flag, defined as follows: Flag 0 indicates sources detected by all the three independent methods used for source extraction making them reliable sources. Flag 1 indicates objects confirmed only after L-wide follow-up observations. Flag 2 indicates objects which are contaminated by RFI: they are in general sure detections but the H I parameters (e.g. flux, velocity width, etc.) can be strongly affected and should not be used.

The AGES source catalogue and the spectra for all the H I sources are publicly available at http://www.naic.edu/∼ages/public_data.html

The results of the LBW follow-up observations are presented in Table 2, which lists the following. Col. 1: H I source ID. Col. 2: heliocentric velocity and relative error of the source (*cz*), measured as the mid-point between the channels at which the flux density drops to 50 per cent. Col. 3: velocity width and relative error of the source line profile measured at the 50 per cent level. The velocity widths are not corrected for instrumental broadening, turbulent motions, disc inclination or cosmological effects. Col. 4: velocity width and relative error of the source line profile measured at the 20 per cent level. Col. 5: total flux and relative error in Jy km s^{-1}. Col. 6: the rms noise per channel at 10 km s^{-1} velocity resolution. In Fig. 2, we compare the measurements obtained using the ALFA and L-wide receivers for the 22 sources confirmed during follow-up observations (filled circles). Although these are the lowest S/N sources within our sample, the agreement between the data set is quite good with an average dispersion of 19 km s^{-1} in recessional velocity, 35 km s^{-1} in velocity width and ∼14 per cent in total flux.

4.1 Comparison with previous works

The Coma-A1367 supercluster is one of the regions most intensively investigated by optically selected H I surveys (i.e. Haynes et al. 1997; Gavazzi et al. 2006). However, only 21 out of the 100 sources detected by AGES had a previous H I measurement. The high number of new H I detections in AGES (∼79 per cent) confirms once more the importance of H I blind surveys for having an unbiased view of the neutral hydrogen distribution in the local Universe. Among the 21 sources previously known (Gavazzi 1989; Haynes et al. 1997; Springob et al. 2005b; Gavazzi et al. 2006), three of these objects (namely CGCG97-079, CGCG97-087 and CGCG127-052) are strongly contaminated by RFIs in the AGES cube, and cannot be used for a comparison with the literature. Our measurements for the remaining 18 objects are in satisfactory agreement with past works as illustrated in Fig. 2 (empty circles). There is quite a good agreement in both fluxes and velocity width measurements, and the average scatter is ∼10 per cent in flux and ∼28 km s^{-1} in velocity width. In one case (CGCG97-138), our velocity width estimate differs considerably from literature values: Gavazzi (1989) gives a velocity width of 160 km s^{-1} whereas we measure only 62 km s^{-1}. However, our new L-wide measurement is consistent with the value obtained from the AGES cube (W=58 km s^{-1}).

4.2 Optical counterparts

The Abell 1367 region has been covered in the optical by the Sloan Digital Sky Survey (SDSS) as part of Data Release 5 (DR5). We have used this homogenous data set to look for optical counterparts of our H I sources. We cross-correlated our list of H I detections with the SDSS galaxy catalogue using a search radius of 4 arcmin. In the few cases in which no candidate optical counterpart was found, we visually inspected the SDSS plates to look for low surface brightness galaxies not included in the SDSS catalogue. Once a candidate optical counterpart was found, we looked into the literature and NASA/IPAC Extragalactic Data base (NED) for an estimate of its optical recessional velocity. In addition, for five of the 46 candidates without an available redshift in the literature, we obtained new optical recessional velocity estimates in 2007 January–February using the imaging spectrograph Bologna Faint Objects Spectrograph attached to the Cassini 1.5 m telescope at Loiano (Italy). Observations and data reduction techniques applied are described in Cortese et al. (2003).

Confirmed optical counterparts are defined as those optical galaxies lying within 4 arcmin and having a recessional velocity within ±200 km s^{-1} from the radio velocity. Candidate optical counterparts are galaxies which lie within 4 arcmin but do not have a published optical recessional velocity. Of the 100 H I sources in our sample, 55 have confirmed optical counterparts, 34 have a unique candidate (i.e. no optical recessional velocity available) optical counterpart, seven have two or more candidate counterparts and four sources appear to have no optical counterparts. Three of these objects are associated with the interacting groups in the outskirts of Abell 1367 described in the Appendix. A list of the optical counterparts (confirmed and candidate) associated with the H I sources is presented in Table 3.

In Fig. 3, we show the distribution of the difference between the optical and H I positions and recessional velocities for the 55 sources having confirmed optical counterparts. Optical and radio measurements show a very good agreement with a median offset of only 18 arcsec in position (consistent with the typical error of 16 arcsec in the estimate of the centroid for radio sources) and of ∼4±16 km s^{-1} in recessional velocity.

For all the H I sources having one optical counterpart (confirmed or candidate), we downloaded SDSS-DR5 *ugriz* images (Adelman-McCarthy et al. 2007) and performed aperture photometry and surface brightness profile decomposition using the task *ellipse* within IRAF. The radial profiles have been constructed by integrating the available images within elliptical, concentric annuli. The ellipticity and position angles have been determined and then fixed using the *i*-band image. Total magnitudes, effective radii (r_e) and effective

Table 1. H I parameters for the 100 sources detected in the Abell 1367 cube.

H I ID	RA (J2000)	σ_{RA} (s)	Dec. (J2000)	$\sigma_{Dec.}$ (arcsec)	V (km s^{-1})	W50 (km s^{-1})	W20 (km s^{-1})	F_{peak} (mJy)	F_{tot} (Jy km s^{-1})	Flag
AGES J113444+201217	11:34:44.4	0.7	20:12:17	11	9602 ± 6	127 ± 12	181 ± 18	5.5 ± 0.7	0.50 ± 0.08	0
AGES J113508+201210	11:35:08.8	0.7	20:12:10	10	16152 ± 7	105 ± 14	137 ± 20	3.5 ± 0.6	0.35 ± 0.08	1
AGES J113523+201823	11:35:23.8	0.7	20:18:23	10	10464 ± 6	300 ± 11	344 ± 17	5.0 ± 0.7	0.71 ± 0.10	0
AGES J113524+200009	11:35:24.2	0.8	20:00:09	13	9523 ± 3	283 ± 7	294 ± 10	3.4 ± 0.5	0.47 ± 0.08	1
AGES J113544+195120	11:35:44.8	0.8	19:51:20	11	6564 ± 7	84 ± 14	120 ± 20	3.7 ± 0.6	0.28 ± 0.07	0
AGES J113553+201308	11:35:53.9	0.7	20:13:08	11	1142 ± 4	62 ± 7	103 ± 11	8.8 ± 0.7	0.51 ± 0.07	0
AGES J113614+195910	11:36:14.3	0.8	19:59:10	13	6713 ± 11	119 ± 22	273 ± 33	4.9 ± 0.6	0.68 ± 0.10	0
AGES J113626+195102	11:36:26.5	0.8	19:51:02	12	6609 ± 9	122 ± 19	204 ± 28	4.8 ± 0.7	0.57 ± 0.10	0
AGES J113641+200622	11:36:41.2	0.7	20:06:22	10	18604 ± 8	276 ± 17	336 ± 25	4.6 ± 0.7	0.89 ± 0.13	0
AGES J113653+200003	11:36:53.7	0.7	20:00:03	11	6637 ± 6	262 ± 12	305 ± 18	4.7 ± 0.6	0.77 ± 0.11	0
AGES J113657+195837	11:36:57.1	0.7	19:58:37	10	6190 ± 3	302 ± 7	394 ± 10	26.6 ± 1.4	6.38 ± 0.28	0
AGES J113718+192129	11:37:18.4	0.7	19:21:29	10	14348 ± 5	328 ± 11	355 ± 16	4.9 ± 0.7	0.95 ± 0.13	0
AGES J113736+200934	11:37:36.0	0.7	20:09:34	11	7739 ± 3	369 ± 7	391 ± 10	8.7 ± 0.9	1.51 ± 0.15	0
AGES J113743+195559	11:37:43.7	0.8	19:55:59	13	7135 ± 8	106 ± 15	144 ± 23	3.4 ± 0.6	0.32 ± 0.08	2
AGES J113801+200106	11:38:01.0	0.8	20:01:06	12	19052 ± 5	314 ± 10	329 ± 15	4.5 ± 0.8	0.90 ± 0.15	1
AGES J113804+195146	11:38:04.5	0.7	19:51:46	10	6203 ± 3	220 ± 6	243 ± 9	8.1 ± 0.7	1.39 ± 0.12	0
AGES J113804+201441	11:38:04.5	1.0	20:14:41	11	7580 ± 4	60 ± 7	80 ± 11	3.7 ± 0.4	0.17 ± 0.04	0
AGES J113805+193250	11:38:05.9	0.7	19:32:50	10	17843 ± 3	331 ± 7	352 ± 10	6.0 ± 0.7	0.91 ± 0.11	0
AGES J113828+195823	11:38:28.5	0.7	19:58:23	11	6989 ± 2	133 ± 4	144 ± 6	7.9 ± 0.7	0.33 ± 0.06	2
AGES J113835+195550	11:38:35.5	1.0	19:55:50	17	13218 ± 6	301 ± 12	334 ± 18	2.7 ± 0.4	0.52 ± 0.07	1
AGES J113842+200527	11:38:42.4	0.8	20:05:27	11	3513 ± 4	28 ± 7	49 ± 11	4.7 ± 0.6	0.13 ± 0.04	0
AGES J113844+200821	11:38:44.8	0.7	20:08:21	10	3113 ± 1	124 ± 3	138 ± 4	25.7 ± 1.4	3.04 ± 0.19	0
AGES J113850+193622	11:38:50.8	1.8	19:36:22	21	6811 ± 6	122 ± 11	196 ± 17	6.1 ± 0.6	0.59 ± 0.07	0
AGES J113904+194129	11:39:04.2	0.7	19:41:29	11	16984 ± 7	161 ± 14	194 ± 21	4.0 ± 0.7	0.29 ± 0.08	1
AGES J113910+193558	11:39:10.3	0.7	19:35:58	10	6783 ± 7	116 ± 13	383 ± 20	15.4 ± 0.9	2.40 ± 0.15	0
AGES J113913+195915	11:39:13.2	1.0	19:59:15	12	10153 ± 6	255 ± 12	292 ± 18	3.5 ± 0.5	0.36 ± 0.07	0
AGES J113922+193232	11:39:22.6	0.8	19:32:32	13	6783 ± 3	252 ± 5	282 ± 8	9.8 ± 0.7	1.58 ± 0.11	0
AGES J113926+194459	11:39:26.7	0.7	19:44:59	15	17182 ± 12	145 ± 23	203 ± 35	2.7 ± 0.6	0.32 ± 0.09	1
AGES J113930+191706	11:39:30.9	0.7	19:17:06	10	3438 ± 3	57 ± 6	85 ± 9	15.3 ± 1.3	0.89 ± 0.12	0
AGES J113936+202020	11:39:36.9	0.7	20:20:20	12	16743 ± 4	358 ± 7	370 ± 11	5.2 ± 0.8	1.03 ± 0.15	0
AGES J113939+193524	11:39:39.5	0.7	19:35:24	10	7382 ± 4	57 ± 8	104 ± 12	8.5 ± 0.7	0.52 ± 0.07	0
AGES J113942+200817	11:39:42.4	0.8	20:08:17	12	16920 ± 9	25 ± 18	185 ± 27	5.3 ± 0.6	0.18 ± 0.04	1
AGES J113945+195341	11:39:45.2	0.7	19:53:41	10	11177 ± 4	74 ± 7	103 ± 11	4.6 ± 0.5	0.32 ± 0.05	0
AGES J113947+195559	11:39:47.3	0.7	19:55:59	10	10933 ± 3	164 ± 6	246 ± 10	24.8 ± 1.3	4.09 ± 0.21	0
AGES J113956+195955	11:39:56.1	0.7	19:59:55	11	10090 ± 4	240 ± 7	248 ± 11	3.1 ± 0.6	0.45 ± 0.09	0
AGES J114016+194715	11:40:16.9	0.7	19:47:15	11	3476 ± 3	68 ± 6	96 ± 9	6.9 ± 0.6	0.45 ± 0.06	0
AGES J114027+192429	11:40:27.5	0.7	19:24:29	10	3411 ± 3	91 ± 5	141 ± 8	26.4 ± 1.4	2.46 ± 0.17	0
AGES J114039+195455	11:40:39.0	0.7	19:54:55	11	7839 ± 3	186 ± 6	214 ± 10	6.7 ± 0.6	0.83 ± 0.09	0
AGES J114113+193240	11:41:13.6	1.0	19:32:40	14	10011 ± 7	260 ± 14	291 ± 20	3.4 ± 0.6	0.50 ± 0.10	1
AGES J114118+200829	11:41:18.0	0.7	20:08:29	11	14616 ± 4	156 ± 7	186 ± 11	5.8 ± 0.6	0.76 ± 0.08	0
AGES J114129+200550	11:41:29.5	1.1	20:05:50	21	14591 ± 8	146 ± 16	194 ± 25	3.0 ± 0.5	0.33 ± 0.07	1
AGES J114131+201912	11:41:31.5	0.9	20:19:12	18	3504 ± 9	23 ± 18	90 ± 26	4.6 ± 0.7	0.11 ± 0.05	1
AGES J114143+193536	11:41:43.4	0.7	19:35:36	10	16787 ± 4	125 ± 8	157 ± 13	6.1 ± 0.7	0.58 ± 0.08	0
AGES J114148+194538	11:41:48.0	0.7	19:45:38	10	7811 ± 6	138 ± 12	201 ± 18	6.0 ± 0.7	0.73 ± 0.09	0
AGES J114204+194536	11:42:04.0	0.7	19:45:36	10	11059 ± 7	172 ± 15	210 ± 22	3.4 ± 0.6	0.35 ± 0.08	1
AGES J114209+201924	11:42:09.3	0.7	20:19:24	10	5764 ± 5	319 ± 9	337 ± 14	5.9 ± 0.9	1.25 ± 0.18	0
AGES J114211+195827	11:42:11.7	0.7	19:58:27	11	7774 ± 6	145 ± 12	246 ± 18	6.8 ± 0.6	0.88 ± 0.09	0
AGES J114216+200302	11:42:16.0	1.5	20:03:02	19	6087 ± 5	112 ± 9	173 ± 14	6.7 ± 0.6	0.74 ± 0.08	0
AGES J114224+200710	11:42:24.4	0.7	20:07:10	10	5979 ± 2	334 ± 3	353 ± 5	17.8 ± 1.0	4.30 ± 0.20	0
AGES J114239+201150	11:42:39.6	0.8	20:11:50	10	5993 ± 8	169 ± 16	263 ± 23	4.6 ± 0.6	0.56 ± 0.08	0
AGES J114243+200143	11:42:43.8	0.7	20:01:43	11	6338 ± 3	300 ± 6	307 ± 10	3.0 ± 0.5	0.46 ± 0.08	0
AGES J114255+195734	11:42:55.9	0.7	19:57:34	10	7264 ± 7	186 ± 13	292 ± 20	7.5 ± 0.7	1.17 ± 0.11	0
AGES J114308+194210	11:43:08.1	0.7	19:42:10	10	12952 ± 5	313 ± 10	371 ± 15	5.9 ± 0.6	1.32 ± 0.11	0
AGES J114311+200032	11:43:11.8	0.7	20:00:32	11	7085 ± 7	65 ± 14	112 ± 21	4.2 ± 0.6	0.25 ± 0.06	2
AGES J114312+193655	11:43:12.0	0.7	19:36:55	10	6247 ± 4	56 ± 8	93 ± 12	7.2 ± 0.7	0.36 ± 0.06	0
AGES J114331+193747	11:43:31.6	0.7	19:37:47	10	13131 ± 4	274 ± 9	341 ± 13	8.2 ± 0.6	1.97 ± 0.13	0
AGES J114347+195820	11:43:47.1	0.7	19:58:20	10	6904 ± 8	165 ± 16	547 ± 25	13.2 ± 0.8	2.65 ± 0.15	2
AGES J114358+200430	11:43:58.5	0.7	20:04:30	10	7372 ± 2	258 ± 4	273 ± 6	12.3 ± 0.9	2.53 ± 0.16	0
AGES J114402+202313	11:44:02.5	0.8	20:23:13	11	11843 ± 6	243 ± 11	274 ± 17	6.4 ± 1.0	0.72 ± 0.13	0
AGES J114416+201309	11:44:16.4	0.8	20:13:09	12	6370 ± 6	302 ± 12	325 ± 18	3.3 ± 0.6	0.55 ± 0.10	0
AGES J114435+192841	11:44:35.6	0.7	19:28:41	10	2765 ± 2	133 ± 3	144 ± 5	8.9 ± 0.7	1.05 ± 0.10	0
AGES J114447+200737	11:44:47.7	0.7	20:07:37	11	6583 ± 3	392 ± 6	408 ± 9	5.1 ± 0.6	0.67 ± 0.08	0

Table 1 – *continued*

H I ID	RA (J2000)	σ_{RA} (s)	Dec. (J2000)	$\sigma_{Dec.}$ (arcsec)	V (km s^{-1})	W50 (km s^{-1})	W20 (km s^{-1})	F_{peak} (mJy)	F_{tot} (Jy km s^{-1})	Flag
AGES J114451+192723	11:44:51.8	0.7	19:27:23	10	5478 ± 8	374 ± 15	456 ± 23	5.2 ± 0.7	1.25 ± 0.13	0
AGES J114452+194635	11:44:52.9	0.7	19:46:35	10	8225 ± 8	261 ± 16	425 ± 25	8.6 ± 0.8	1.46 ± 0.14	0
AGES J114503+195832	11:45:03.2	0.7	19:58:32	10	5091 ± 2	465 ± 4	494 ± 6	18.8 ± 1.1	6.37 ± 0.26	0
AGES J114508+200837	11:45:08.5	0.7	20:08:37	11	3724 ± 2	74 ± 5	95 ± 7	9.6 ± 0.8	0.62 ± 0.08	0
AGES J114543+200147	11:45:43.5	0.7	20:01:47	10	5322 ± 2	45 ± 4	80 ± 6	38.0 ± 2.0	1.56 ± 0.16	0
AGES J114545+194210	11:45:45.9	0.8	19:42:10	12	6182 ± 7	154 ± 14	183 ± 21	3.1 ± 0.6	0.33 ± 0.08	1
AGES J114612+202403	11:46:12.4	0.7	20:24:03	11	7026 ± 3	595 ± 7	610 ± 10	9.4 ± 1.2	2.39 ± 0.24	2
AGES J114625+193024	11:46:25.5	0.7	19:30:24	10	2189 ± 3	103 ± 5	121 ± 8	6.0 ± 0.6	0.54 ± 0.07	0
AGES J114638+194854	11:46:38.1	0.9	19:48:54	14	5416 ± 9	97 ± 19	149 ± 28	2.7 ± 0.5	0.21 ± 0.06	1
AGES J114646+191906	11:46:46.8	0.7	19:19:06	11	14644 ± 9	173 ± 18	277 ± 28	7.2 ± 1.0	0.96 ± 0.14	0
AGES J114724+192324	11:47:24.1	0.7	19:23:24	10	5854 ± 4	159 ± 7	175 ± 11	4.8 ± 0.6	0.52 ± 0.09	0
AGES J114727+194906	11:47:27.4	0.8	19:49:06	11	5869 ± 7	60 ± 15	99 ± 22	3.6 ± 0.6	0.19 ± 0.06	1
AGES J114730+195353	11:47:30.0	0.8	19:53:53	14	5759 ± 5	261 ± 11	282 ± 16	3.7 ± 0.6	0.41 ± 0.08	1
AGES J114739+195621	11:47:39.7	0.7	19:56:21	10	6173 ± 2	386 ± 4	396 ± 6	7.1 ± 0.7	1.29 ± 0.12	0
AGES J114739+200924	11:47:39.2	0.7	20:09:24	10	5316 ± 5	124 ± 11	156 ± 16	3.7 ± 0.5	0.37 ± 0.07	0
AGES J114809+192109	11:48:09.1	2.4	19:21:09	18	11252 ± 5	171 ± 9	179 ± 14	3.3 ± 0.8	0.34 ± 0.10	1
AGES J114823+194244	11:48:23.1	0.7	19:42:44	10	5079 ± 7	82 ± 14	155 ± 21	4.5 ± 0.5	0.25 ± 0.05	1
AGES J114824+202331	11:48:24.3	0.9	20:23:31	17	6750 ± 8	80 ± 15	143 ± 23	9.8 ± 1.4	0.64 ± 0.14	0
AGES J114829+194529	11:48:29.3	1.1	19:45:29	11	5586 ± 4	121 ± 8	144 ± 13	5.7 ± 0.8	0.41 ± 0.08	0
AGES J114956+192840	11:49:56.7	0.8	19:28:40	11	6139 ± 4	67 ± 7	82 ± 11	3.9 ± 0.5	0.23 ± 0.05	1
AGES J115030+200505	11:50:30.0	0.8	20:05:05	11	6021 ± 7	161 ± 14	185 ± 21	2.9 ± 0.6	0.27 ± 0.08	1
AGES J115034+194301	11:50:34.4	0.7	19:43:01	10	6633 ± 7	88 ± 15	162 ± 22	5.2 ± 0.7	0.38 ± 0.07	0
AGES J115052+193102	11:50:52.7	0.7	19:31:02	11	11829 ± 8	270 ± 16	336 ± 24	3.7 ± 0.5	0.67 ± 0.09	0
AGES J115101+193728	11:51:01.0	0.7	19:37:28	11	11626 ± 4	247 ± 8	268 ± 12	4.3 ± 0.5	0.53 ± 0.08	0
AGES J115101+202355	11:51:01.8	0.7	20:23:55	10	6453 ± 2	269 ± 4	284 ± 5	21.8 ± 1.5	3.45 ± 0.24	0
AGES J115120+192931	11:51:20.4	0.8	19:29:31	10	11971 ± 4	201 ± 9	226 ± 13	4.2 ± 0.5	0.42 ± 0.07	0
AGES J115147+192057	11:51:47.4	0.7	19:20:57	11	6931 ± 3	343 ± 6	354 ± 9	5.1 ± 0.7	0.61 ± 0.09	2
AGES J115150+194720	11:51:50.7	1.0	19:47:20	14	6361 ± 4	102 ± 9	119 ± 13	3.2 ± 0.5	0.23 ± 0.06	1
AGES J115156+193838	11:51:56.1	0.7	19:38:38	10	6060 ± 2	187 ± 5	212 ± 7	11.7 ± 0.8	1.58 ± 0.12	0
AGES J115202+193423	11:52:02.3	0.7	19:34:23	10	11989 ± 5	163 ± 10	186 ± 15	3.3 ± 0.5	0.33 ± 0.07	0
AGES J115223+201943	11:52:23.5	0.7	20:19:43	12	6491 ± 5	128 ± 10	180 ± 15	8.6 ± 0.9	0.95 ± 0.12	0
AGES J115227+200821	11:52:27.9	0.7	20:08:21	10	16085 ± 7	140 ± 14	167 ± 20	3.2 ± 0.6	0.35 ± 0.08	1
AGES J115250+201423	11:52:50.5	0.7	20:14:23	10	14678 ± 3	186 ± 6	218 ± 10	10.2 ± 0.9	1.64 ± 0.14	0
AGES J115318+200622	11:53:18.0	0.7	20:06:22	10	6215 ± 3	112 ± 5	163 ± 8	19.7 ± 1.1	2.01 ± 0.14	0
AGES J115349+194505	11:53:49.8	0.7	19:45:05	10	12047 ± 6	447 ± 12	493 ± 17	6.0 ± 0.8	1.28 ± 0.14	0
AGES J115356+201043	11:53:56.2	0.8	20:10:43	11	15210 ± 4	228 ± 8	236 ± 11	3.7 ± 0.7	0.49 ± 0.11	1-2
AGES J115358+195734	11:53:58.9	0.7	19:57:34	11	15336 ± 9	125 ± 17	193 ± 26	4.0 ± 0.6	0.43 ± 0.08	2
AGES J115414+200138	11:54:14.1	0.7	20:01:38	11	6208 ± 3	225 ± 7	249 ± 10	10.0 ± 1.0	1.50 ± 0.16	0

surface brightness (μ_e, i.e. average surface brightness within r_e) have been determined following the procedure of Gavazzi et al. (2000).

4.3 Comparison with other H I blind surveys

Fig. 4 illustrates the sky (upper panel) and the H I mass versus distance distributions (lower panel) for all the 100 sources detected in the A1367 cube. Over half of the sources (54) belong to the Abell 1367 cluster and its outskirts, lying in the velocity range $4000 < V < 9000\,\mathrm{km\,s^{-1}}$. This roughly explains why in this cube we detect twice the number of sources than in other AGES fields: excluding the Abell 1367 region ($4000 < V < 9000$), we are left with 46 sources consistent with the number found in NGC 628 (Auld et al. 2006), NGC 1156 (Auld et al., in preparation) and NGC 7332 (Minchin et al. 2006). The bottom panel of Fig. 4 allows a direct comparison of AGES with ALFALFA (Giovanelli et al. 2005) showing that, in the same area of sky, ALFALFA would miss approximately half of the sources detected here. This is quite expected since ALFALFA has an integration time ∼6.3 times shorter (∼48 s instead of ∼300 s) than AGES. More impressive is the difference between AGES and the northern HIPASS extension (Wong et al. 2006): whereas AGES finds 100 sources, HIPASS does not detect a single galaxy in the 5×1 deg^2 studied here.

5 PHYSICAL PROPERTIES OF THE AGES-A1367 SAMPLE

We use the H I data from AGES and the optical data from SDSS to derive the physical properties of our sample. The H I mass [M(H I)] is defined as

$$M(\mathrm{H\,I}) = 2.36 \times 10^5 D^2 F_{tot} \qquad (\mathrm{M_\odot}), \tag{2}$$

where F_{tot} is the integrated H I flux in Jy km s^{-1} and D is the galaxy distance in Mpc. For those galaxies belonging to Abell 1367 ($4000 < V < 9000\,\mathrm{km\,s^{-1}}$), we assume $D = 92.8$ Mpc (Sakai et al. 2000) while we assume $D = V/H_0$ with $H_0 = 70\,\mathrm{km\,s^{-1}Mpc^{-1}}$ for the rest of the sample. The stellar mass is obtained from the optical colours and luminosity as defined in Bell et al. (2003b):

$$\log(M_{star}) = -0.222 + 0.864(g-r) + \frac{M(i) - 4.56}{-2.5} \qquad (\mathrm{M_\odot}), \tag{3}$$

Table 2. H I parameters for the 22 sources observed with L-wide and confirmed.

H I ID	V (km s^{-1})	W50 (km s^{-1})	W20 (km s^{-1})	$F_{\rm tot}$ (Jy km s^{-1})	rms (mJy)
AGES J113508+201210	16144 ± 6	99 ± 12	128 ± 18	0.37 ± 0.08	0.77
AGES J113524+200009	9556 ± 7	303 ± 13	340 ± 20	0.40 ± 0.07	0.52
AGES J113801+200106	19086 ± 11	243 ± 22	372 ± 33	0.89 ± 0.12	0.80
AGES J113835+195550	13198 ± 5	286 ± 9	294 ± 14	0.52 ± 0.12	0.80
AGES J113904+194129	16917 ± 10	54 ± 19	113 ± 29	0.22 ± 0.07	0.70
AGES J113926+194459	17186 ± 7	167 ± 15	203 ± 22	0.45 ± 0.10	0.80
AGES J113942+200817	16915 ± 7	25 ± 14	87 ± 21	0.13 ± 0.05	0.80
AGES J114113+193240	10008 ± 9	256 ± 19	297 ± 28	0.45 ± 0.11	0.75
AGES J114129+200550	14584 ± 7	161 ± 14	190 ± 21	0.22 ± 0.06	0.54
AGES J114131+201912	3506 ± 6	68 ± 12	98 ± 17	0.22 ± 0.06	0.80
AGES J114204+194536	11066 ± 15	134 ± 30	225 ± 45	0.22 ± 0.07	0.55
AGES J114545+194210	6168 ± 10	147 ± 20	181 ± 30	0.26 ± 0.08	0.58
AGES J114638+194854	5421 ± 12	113 ± 23	184 ± 34	0.18 ± 0.06	0.55
AGES J114727+194906	5864 ± 7	86 ± 13	113 ± 19	0.19 ± 0.05	0.52
AGES J114730+195353	5765 ± 13	176 ± 26	287 ± 38	0.36 ± 0.08	0.52
AGES J114809+192109	11249 ± 9	71 ± 18	128 ± 26	0.18 ± 0.06	0.72
AGES J114823+194244	5078 ± 8	67 ± 16	102 ± 24	0.24 ± 0.08	0.75
AGES J114956+192840	6136 ± 4	76 ± 8	87 ± 11	0.09 ± 0.04	0.52
AGES J115030+200505	6022 ± 4	177 ± 8	247 ± 12	0.28 ± 0.02	0.60
AGES J115150+194720	6357 ± 4	104 ± 8	115 ± 12	0.25 ± 0.07	0.76
AGES J115227+200821	16091 ± 7	164 ± 14	211 ± 21	0.34 ± 0.07	0.56
AGES J115356+201043	15197 ± 5	228 ± 10	248 ± 14	0.47 ± 0.09	0.80

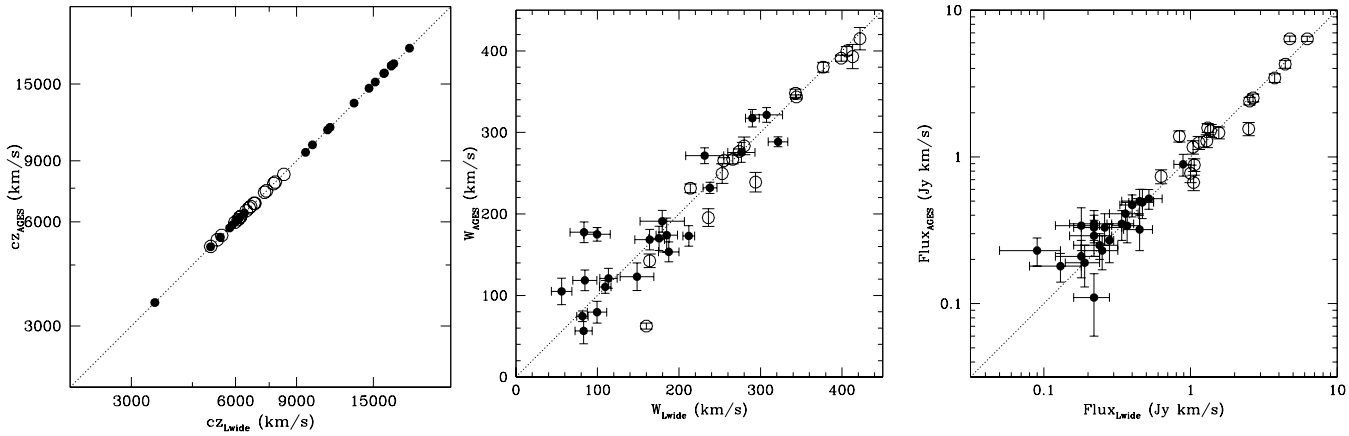

Figure 2. Comparison of the recessional velocities (left-hand panel), the velocity widths (centre) and the H I fluxes measured by AGES and L-wide. Filled circles indicate the 22 sources confirmed during follow-up observations and empty circles show the 18 galaxies already known from the literature . The dotted lines indicate a one-to-one correlation.

where $M(i)$ is the absolute magnitude in the i band. Therefore, the total amount of baryons is $M_{\rm bar} = M_{\rm star} + M({\rm H\,I})$ (e.g. Bell et al. 2003a). This quantity does not include the contribution of helium and metals [usually assumed equal to 1.4 × M(H I)], the molecular hydrogen and any warm or hot gas component. Therefore, $M_{\rm bar}$ must be considered as a lower limit of the real value. Finally, we define the galaxy dynamical mass as

$$M_{\rm dyn} = \gamma \frac{R_{75} W_c^2}{4G}, \tag{4}$$

where G is the gravitational constant, R_{75} is the radius containing 75 per cent of the i-band flux, W_c is the H I velocity width (here we use the average between W_{50} and W_{20} H I velocity widths) corrected for inclination and γ is the ratio between R_{75} and the extension of the H I emission (i.e. $\gamma = R_{\rm H\,I}/R_{75}$). γ should lie between 2 and 3 (Salpeter & Hoffman 1996; Swaters et al. 2002), but for our galaxies radio interferometric data (necessary to estimate $R_{\rm H\,I}$) are not available, so this remains unknown and we leave it as a free parameter. The galaxy inclination is obtained from the ellipticity determined in the i band via

$$\cos(i)^2 = \frac{(1-e)^2 - q_0^2}{1 - q_0^2}, \tag{5}$$

where e is the galaxy ellipticity and q_0 is the intrinsic axial ratio of the galaxy, here assumed equal to 0.13 (Giovanelli et al. 1997). We excluded from this analysis face-on galaxies having $e < 0.1$ (20 galaxies), for which it is not possible to accurately estimate the dynamical mass.

The correlations between different optical and H I quantities and their distributions for our sample are presented in Fig. 5. From

Table 3. List of optical counterparts for the 100 H I sources in A1367.

H I ID	Optical ID	RA (J2000)	Dec. (J2000)	Optical velocity (km s^{-1})
AGES J113444+201217	MAPS-NGPO_434_0001768	11:34:46.01	20:12:17.2	9652*
AGES J113508+201210	SDSSJ113508.79+201216.1	11:35:08.79	20:12:16.1	–
AGES J113523+201823	KUG1132+205	11:35:23.13	20:18:42.4	10451
AGES J113524+200009	MAPS-NGPO_375_1208433	11:35:27.77	20:00:2.7	–
AGES J113544+195120	SDSSJ113544.31+195114.0	11:35:44.31	19:51:14	–
AGES J113553+201308	KUG1133+204	11:35:54.44	20:13:19.9	1097*
AGES J113614+195910	–	–	–	–
AGES J113626+195102	–	–	–	–
AGES J113641+200622	MAPS-NGPO_434_0002451	11:36:41.66	20:06:38.9	–
AGES J113653+200003	KUG1134+202A	11:36:54.24	19:59:49.9	6630
AGES J113657+195837	UGC06583	11:36:54.40	19:58:15.0	6191
AGES J113718+192129	KUG1134+196	11:37:17.60	19:21:36.0	14370
AGES J113736+200934	CGCG097-033	11:37:36.00	20:09:49.0	7736
AGES J113743+195559	SDSSJ113744.57+195556.7	11:37:44.57	19:55:56.7	–
	SDSSJ113744.21+195616.2	11:37:44.21	19:56:16.2	–
	SDSSJ113743.51+195555.4	11:37:43.51	19:55:55.4	–
AGES J113801+200106	SDSS J113804.47+200021.8	11:38:04.47	20:00:21.8	–
	SDSS J113804.46+200043.4	11:38:04.46	20:00:43.4	–
AGES J113804+195146	2MASXJ11380386+1951420	11:38:03.90	19:51:41.0	6196
AGES J113804+201441	MAPS-NGPO_434_0002980	11:38:00.73	20:14:32.3	–
AGES J113805+193250	2MASXJ11380463+1933020	11:38:05.00	19:33:01.0	17891
AGES J113828+195823	LSBCD571-03	11:38:28.16	19:58:50.1	6981
AGES J113835+195550	2MASXJ11383847+1954564	11:38:38.49	19:54:56.7	–
AGES J113842+200527	SDSSJ113845.65+200511.4	11:38:45.65	20:05:11.4	–
AGES J113844+200821	KUG1136+204	11:38:45.26	20:08:24.1	3131*
AGES J113850+193622	KUG1136+198	11:38:51.00	19:36:04.0	6787
AGES J113904+194129	SDSSJ113906.75+194135.1	11:39:06.75	19:41:35.1	–
AGES J113910+193558	FGC1287	11:39:10.95	19:35:06.0	6825
AGES J113913+195915	MAPS-NGPO_434_0016203	11:39:11.00	19:59:00.9	–
AGES J113922+193232	CGCG097-041	11:39:24.50	19:32:04.0	6778
AGES J113926+194459	KUG1136+200	11:39:28.71	19:44:12.1	–
AGES J113930+191706	MAPS-NGPO_434_0045678	11:39:31.78	19:17:24.9	–
AGES J113936+202020	2MASXJ11393700+2020039	11:39:37.00	20:20:03.9	–
AGES J113939+193524	SDSSLSB	11:39:40.17	19:35:20.0	–
AGES J113942+200817	SDSSJ113945.23+200806.9	11:39:45.23	20:08:07.0	–
AGES J113945+195341	KUG1137+201A	11:39:44.85	19:53:57.8	–
AGES J113947+195559	UGC06625	11:39:47.60	19:55:60.0	10964
AGES J113956+195955	KUG1137+202B	11:39:57.20	20:00:13.0	10098
AGES J114016+194715	[IBG2003]J114017+194718	11:40:17.26	19:47:19.1	–
AGES J114027+192429	KUG1137+196	11:40:26.15	19:24:51.9	3421
AGES J114039+195455	[IBC2002]J114038+195437	11:40:38.99	19:54:38.5	7784
AGES J114113+193240	KUG1138+198	11:41:13.43	19:32:21.7	10011
AGES J114118+200829	KUG 1138+204	11:41:17.45	20:08:33.4	14500
AGES J114129+200550	SDSSJ114130.18+200629.8	11:41:30.18	20:06:29.8	–
	SDSSJ114129.01+200550.4	11:41:29.01	20:05:50.4	–
	SDSSJ114129.74+200506.0	11:41:29.74	20:05:06.0	–
AGES J114131+201912	SDSSJ114134.75+201917.9	11:41:34.75	20:19:17.9	–
	SDSSJ114128.58+201803.8	11:41:28.58	20:18:03.8	–

left- to right-hand panel: the ratio of the gas to stellar mass, the baryon fraction ($M_{\rm bar}/M_{\rm dyn}$), the total H I mass, the effective surface brightness in i band, the $g-i$ colour and the dynamical mass are presented. Only galaxies with one optical counterpart and $e < 0.1$ (69 galaxies) are shown: filled dots are objects with confirmed optical counterparts while empty dots indicate objects with optical counterpart candidates. Our sample covers almost three orders of magnitude in both H I and dynamical mass. The optical surface brightness distribution shows a significant tail at low surface brightness [$\mu(i)_{\rm e} \sim 22.5$–24 mag arcsec^{-2}] as usually observed in H I selected sample (e.g. Spitzak & Schneider 1998). H I selected samples are often considered as composed of only blue, gas-rich galaxies. This is not the case for our sample which spans over 1 mag in the $g-i$ colour, as is typically observed in optically selected samples (Baldry et al. 2004), and covers a wide range of gas to stars ratios ($M_{\rm gas}/M_{\rm star}$): from gas-poor objects ($M_{\rm gas}/M_{\rm star} \sim 0.1$) to extremely gas rich galaxies ($M_{\rm gas}/M_{\rm star} \sim 10$). More massive galaxies appear to be redder, have higher surface brightness and lower gas content than dwarf systems. This is also found to be the case in optically selected samples (Gavazzi et al. 1996). Well-known relations like colour–mass, surface brightness–mass and hydrogen–dynamical mass are here rediscovered. Unfortunately, the small number of objects in

Table 3 – *continued*

H I ID	Optical ID	RA (J2000)	Dec. (J2000)	Optical velocity ($km\,s^{-1}$)
AGES J114143+193536	MAPS-NGPO_434_0037838	11:41:43.22	19:35:26.2	–
AGES J114148+194538	[IBC2002]J114149+194605	11:41:49.83	19:46:04.4	7789
AGES J114204+194536	SDSSJ114205.74+194611.7	11:42:05.74	19:46:11.7	–
AGES J114209+201924	NGC 3821	11:42:09.09	20:18:56.6	5788
AGES J114211+195827	KUG1139+202	11:42:14.77	19:58:35.2	7815
AGES J114216+200302	KUG1139+203	11:42:15.66	20:02:55.5	6102
AGES J114224+200710	CGCG097-068	11:42:24.48	20:07:09.9	5974
AGES J114239+201150	–	–	–	–
AGES J114243+200143	CGCG097-072	11:42:45.21	20:01:56.6	6332
AGES J114255+195734	CGCG097-073	11:42:56.46	19:57:58.4	7275
AGES J114308+194210	KUG1140+199	11:43:07.96	19:41:57.4	12988
AGES J114311+200032	CGCG097-079	11:43:13.32	20:00:17.5	7000
AGES J114312+193655	[IBC2002]J114313+193645	11:43:13.02	19:36:46.6	6121
AGES J114331+193747	CGCG097-083	11:43:31.22	19:37:40.6	13126
AGES J114347+195820	UGC06697	11:43:49.11	19:58:06.2	6725
AGES J114358+200430	NGC 3840	11:43:59.01	20:04:37.3	7368
AGES J114402+202313	2MASXJ11435706+2022383	11:44:01.92	20:22:51.6	11962
AGES J114416+201309	CGCG097-102	11:44:17.22	20:13:23.9	6368
AGES J114435+192841	MAPS-NGPO_434_0047286	11:44:36.39	19:28:40.1	–
AGES J114447+200737	UGC06719	11:44:47.12	20:07:30.2	6571
AGES J114451+192723	NGC 3859	11:44:52.24	19:27:15.2	5468
AGES J114452+194635	CGCG097-125	11:44:54.85	19:46:34.9	8271
AGES J114503+195832	NGC 3861	11:45:03.87	19:58:25.1	5085
AGES J114508+200837	[IBG2003] J114506+200849	11:45:06.40	20:08:49.2	3822
AGES J114543+200147	CGCG097-138	11:45:44.67	20:01:51.6	5313
AGES J114545+194210	[IBG2003]J114545+194130	11:45:45.27	19:41:30.7	6123
AGES J114612+202403	NGC 3884	11:46:12.19	20:23:29.9	6946
AGES J114625+193024	SDSSJ114626.45+193011.9	11:46:26.45	19:30:11.9	–
AGES J114638+194854	SDSSJ114636.47+194834.1	11:46:36.47	19:48:34.1	–
	SDSSJ114640.32+194820.8	11:46:40.32	19:48:20.8	–
AGES J114646+191906	2MASXJ11464700+1919462	11:46:47.03	19:19:46.2	–
AGES J114724+192324	MAPS-NGPO_434_0048296	11:47:25.08	19:23:31.4	–
AGES J114727+194906	SDSSJ114730.39+194859.0	11:47:30.39	19:48:59.0	–
AGES J114730+195353	2MASXJ11473099+1952201	11:47:30.99	19:52:20.8	5778
AGES J114739+195621	CGCG097-152	11:47:39.35	19:56:22.0	6166
AGES J114739+200924	SDSSJ114737.57+200900.6	11:47:37.57	20:09:00.6	–
AGES J114809+192109	–	–	–	–
AGES J114823+194244	SDSSJ114825.21+194217.0	11:48:25.21	19:42:17.0	–
AGES J114824+202331	LSBCD571-02	11:48:26.40	20:23:19.0	6796
AGES J114829+194529	MAPS-NGPO_434_0031444	11:48:28.43	19:45:36.0	–
AGES J114956+192840	SDSSJ114956.75+192840.4	11:49:56.76	19:28:40.4	–
	SDSSJ114956.93+192830.7	11:49:56.93	19:28:30.7	–
AGES J115030+200505	MAPS-NGPO_434_0021239	11:50:29.99	20:05:08.2	–
AGES J115034+194301	SDSSJ115033.61+194250.1	11:50:33.61	19:42:50.1	–
AGES J115052+193102	KUG1148+197A	11:50:52.48	19:31:10.8	–
AGES J115101+193728	2MASXJ11510128+1937311	11:51:01.29	19:37:31.3	–
AGES J115101+202355	UGC06821	11:51:01.12	20:23:57.3	6438
AGES J115120+192931	KUG1148+197	11:51:21.28	19:29:33.9	–
AGES J115147+192057	KUG1149+196	11:51:48.37	19:21:29.3	6932
AGES J115150+194720	SDSSJ115150.33+194702.6	11:51:50.33	19:47:02.7	–
	SDSSJ115150.87+194613.2	11:51:50.87	19:46:13.2	–
AGES J115156+193838	KUG1149+199	11:51:55.65	19:38:45.4	6134*
AGES J115202+193423	SDSSJ115203.86+193425.5	11:52:03.86	19:34:25.5	–
AGES J115223+201943	KUG1149+206	11:52:24.44	20:19:28.8	6491
AGES J115227+200821	2MASXJ11522887+2007597	11:52:28.85	20:07:59.5	–
AGES J115250+201423	KUG1150+205	11:52:51.04	20:14:21.9	14679
AGES J115318+200622	KUG1150+203	11:53:18.28	20:06:26.6	6061*
AGES J115349+194505	CGCG097-176	11:53:50.34	19:45:01.5	12005
AGES J115356+201043	MAPS-NGPO_376_4233155	11:53:55.94	20:10:55.6	–
AGES J115358+195734	KUG1151+202	11:53:59.89	19:57:27.1	15489
AGES J115414+200138	KUG1151+203	11:54:13.94	20:01:39.0	6187

*New optical redshift obtained in 2007 Winter using the Loiano 1.5 m telescope.

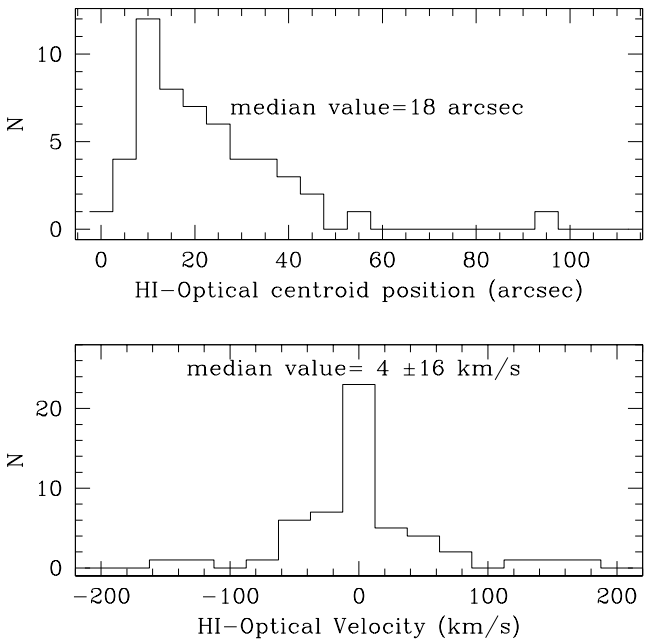

Figure 3. Distribution of the positional (upper panel) and recessional velocity (lower panel) difference between the H I sources and their optical counterparts.

our sample does not allow a more detailed comparison between the slopes, scatters and distributions of the relations followed by H I and optically selected galaxies. We postpone this kind of analysis to the moment when we will have a significantly large AGES data base at our disposition.

The most intriguing result presented in Fig. 5 is the absence of any correlation involving the baryon fraction. On the contrary, all galaxies in our sample appear to have almost the same baryon fraction $\langle \log (M_{\rm bar}/M_{\rm dyn})\rangle = (-0.2 - \log(\gamma)) \pm 0.13$ independently from their mass, surface brightness or gas content. The little dispersion in the baryon fraction distribution is in fact well within the observational errors. Assuming 0.1 dex error in the H I mass (see Section 4.1), in the stellar mass (Bell et al. 2003b) and in the dynamical mass, the uncertainty on the estimate of the baryon fraction is ∼0.17 dex. The gas and stellar mass fraction cover a larger dynamical range (i.e. have a larger dispersion: $\langle \log(M_{\rm star}/M_{\rm dyn})\rangle = (-0.4 - \log(\gamma)) \pm 0.24$ and $\langle \log(M({\rm H\,I})/M_{\rm dyn})\rangle = (-0.6 - \log(\gamma)) \pm 0.3$) than the baryon fraction, as shown in Fig. 6 and according to the Kolmogorov–Smirnov test the baryon fraction distribution is not compatible with the gas and star fraction distributions at a 99.99 per cent confidence level.

We can therefore conclude that our sample shows approximately the same baryon fraction. A constant baryonic mass fraction in galaxies implies a direct correlation between dynamical mass and baryonic mass: exactly what is usually required for the Tully–Fisher relation (McGaugh & de Blok 1998; McGaugh et al. 2000). This result is also consistent with the recent study of an optically selected sample of extremely low mass dwarf galaxies carried out by Geha et al. (2006). To our knowledge, this is the first confirmation of a constant baryonic fraction coming from a H I selected sample. This observational evidence is also consistent with models of galaxy formation (Bullock et al. 2001; Crain et al. 2007) but in contradiction with recent models of galaxy evolution which invoke supernova feedback and other physical mechanisms to remove baryons preferentially from low-mass systems and to reproduce the observed scaling relations (Cole et al. 2000; Governato et al. 2007). Even if our sample includes low surface brightness galaxies, it appears that physical mechanisms that preferentially remove baryons from low-mass galaxies are not effective in the mass range and selection criteria of our sample. We remark that the only way to obtain a correlation between the baryon fraction and the dynamical mass in our sample would be to assume that γ (i.e. the ratio of the H I to optical radius) is a strong function of the mass, and/or the contribution of molecular hydrogen, hot and warm gas to the

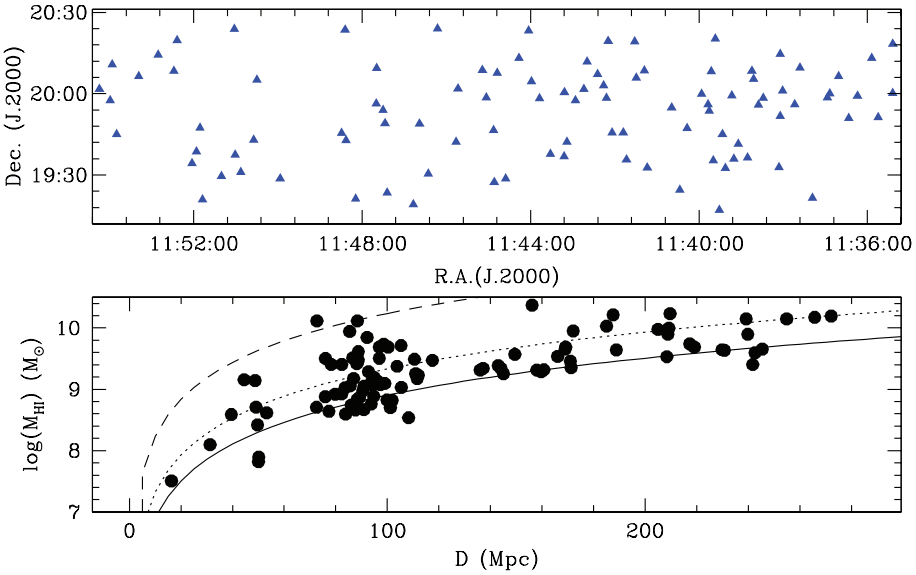

Figure 4. The sky (upper panel) and H I mass versus distance (lower panel) distribution for the 100 H I sources in our sample. In the lower panel, distances are obtained from the recessional velocities assuming that all galaxies are in the Hubble flow. The solid line shows the sensitivity limit for a $S/N_{\rm tot} \sim 6.5$ source having W_{50} of 200 km s^{-1}. The dotted line shows the ALFALFA reliability limit for the same velocity width (Giovanelli et al. 2007). The dashed line indicates a flux integral of 7.3 Jy km s^{-1}, which corresponds to the HIPASS 6.5σ limit for a velocity width of 200 km s^{-1}.

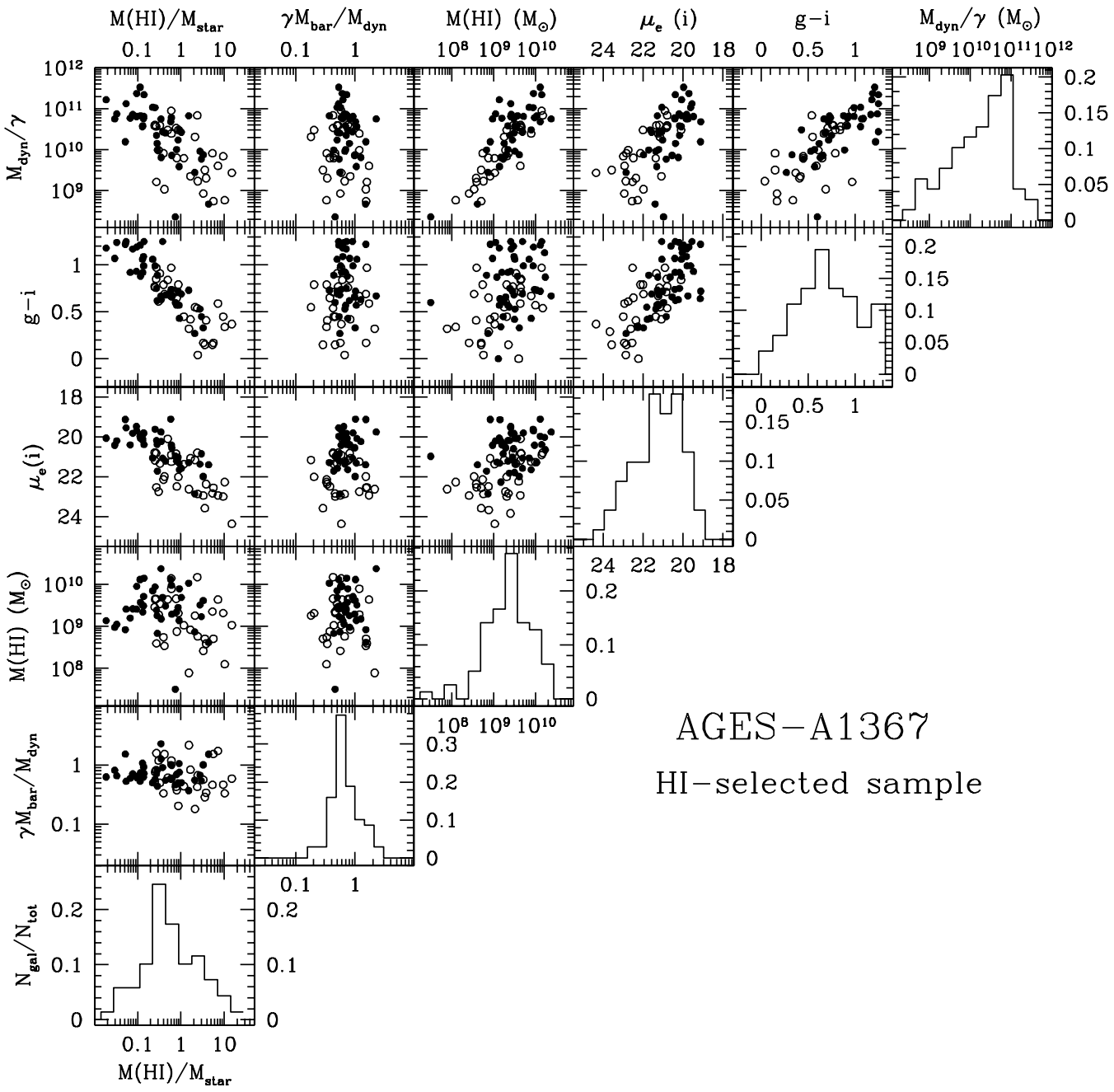

Figure 5. Distributions and correlations between H I and optical properties for the 69 galaxies in our sample having 1 optical counterpart and $e > 0.1$. From left- to right-hand panel, the ratio of the gas to stellar mass, the baryons fraction, the total H I mass, the effective surface brightness in i band, the $g - i$ colour and the dynamical mass are presented. Filled dots are objects with confirmed optical counterparts while empty dots indicate objects with optical counterpart candidates.

total baryon mass varies with the mass of the galaxy. We cannot a priori exclude the first possibility, even if unlikely since Cayatte et al. (1994) found that the ratio of the H I to optical radius varies by only 20 per cent along the Hubble sequence. Conversely, the molecular hydrogen represents only ∼15 per cent of the total gas reservoir in normal, late-type galaxies (Boselli, Lequeux & Gavazzi 2002) and the contribution of hot and warm gas components is a few per cent (⩽1–2 per cent) of the total gas mass (e.g. Tschöke et al. 2001; Higdon et al. 2006), making the second scenario extremely unlikely.

6 COMPARING THE OPTICAL AND H I VIEW OF THE ABELL CLUSTER 1367

More than half of the H I sources detected in the cube belong to the Abell 1367 volume. This includes not only the cluster core but also a part of the Great Wall: a large-scale filament of galaxies connecting Abell 1367 to the Coma cluster (Zabludoff et al. 1993). All galaxies in the filament lie approximately at the same distance from us as Abell 1367, implying that the system A1367+Great Wall constitutes a volume-limited sample. At the distance of Abell 1367

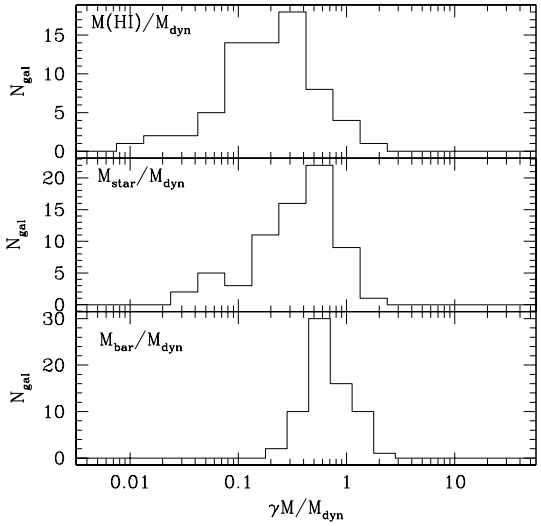

Figure 6. The distribution of the gas to dynamical mass (top), star to dynamical mass (middle) and baryon to dynamical mass (bottom) ratios for our sample.

(∼92.8 Mpc), the surveyed sky area has a physical size of 8.1 × 1.6 Mpc^{-2} and our sensitivity limit for a source with $W_{50} = 200\,\mathrm{km\,s^{-1}}$ is $\sim 6 \times 10^8\,\mathrm{M}_\odot$. Since the virial radius of Abell 1367 is ∼2.3 Mpc (Girardi et al. 1998), our region covers the cluster virialized region and its immediate neighbourhood.

In order to compare the H I and optical properties of the Abell 1367 region, we extracted an optically selected sample of galaxies from SDSS-DR5. We select all galaxies in the AGES region having $g < 17$ mag (corresponding to $L_g > 2 \times 10^9\,\mathrm{L}_\odot$ at the Abell 1367 distance): 259 galaxies in total, of which 208 have optical redshift available and 155 are confirmed cluster members ($4000 < V < 9000\,\mathrm{km\,s^{-1}}$).

We note that the time necessary to carry out a H I targeted survey of this optically selected sample (reaching the same AGES noise level) would be similar to the observing time needed by AGES to cover all the 5 × 1 deg^2 in Abell 1367.

6.1 Sky distribution

The sky distribution of the 54 H I sources belonging to the A1367 region ($4000 < V < 9000\,\mathrm{km\,s^{-1}}$) is shown in Fig. 7. It is interesting to note that no significant overdensity of sources is observed corresponding to the cluster centre: the only H I galaxy lying well within the X-ray cluster contours belongs to a small group of galaxies infalling for the first time into the cluster, suggesting that it is just entering the cluster and it is only projected on the centre of Abell 1367 (Cortese et al. 2006). This appears much more evident when we compare the sky distribution of our sample with the typical sky distribution obtained for the optically selected sample. In Fig. 7, we show the distribution of the 155 confirmed cluster members (empty circles) and of the 51 galaxies without redshift available[3] (empty stars) extracted from the optically selected sample.

The optically selected sample is strongly clustered on the cluster centre and almost half of the sources detected lie within the X-ray emitting region. Moreover, the 'Finger of God' feature, typical of clusters of galaxies, is not observed in the H I selected sample (see Fig. 8). Conversely, the H I selected galaxies show a different pattern in the wedge diagram shown in Fig. 8: galaxies on the east side of the cluster have a lower recessional velocity than galaxies on the west side. This probably suggests the presence of two different infalling directions into the cluster core as proposed by Cortese et al. (2004).

The differences observed between the optically and H I selected samples are somehow expected since clusters of galaxies are made H I deficient structures through the combination of the morphology–density relation (Dressler 1980; Whitmore, Gilmore & Jones 1993) and of the 'gas–density' relation (Giovanelli & Haynes 1985; Gavazzi et al. 2006). This is also consistent with recent determinations of the correlation function for H I selected samples (Basilakos et al. 2007; Meyer et al. 2007), which show that H I galaxies are among the least-clustered objects in the Universe.

The influence of the harsh cluster environment is barely visible when we look for radial variations of the gas to star mass ratio and of the H I deficiency (see Fig. 9). The H I deficiency is defined as the difference, in logarithmic units, between the observed H I mass and the value expected from an isolated galaxy with the same morphological type T and optical linear diameter D: H I DEF = $\langle \log M_{\mathrm{H\,I}}(T^{\mathrm{obs}}, D^{\mathrm{obs}}_{\mathrm{opt}}) \rangle - \log M^{\mathrm{obs}}_{\mathrm{H\,I}}$ (Haynes & Giovanelli 1984). We used the equations in Solanes, Giovanelli & Haynes (1996) to calculate the expected H I mass from the optical diameter. The H I deficiency does not significantly vary with the cluster-centric distance (Fig. 9, bottom panel), contrary to what was usually observed in optically selected samples (i.e. Haynes & Giovanelli 1984; Solanes et al. 2001; Gavazzi et al. 2006). A slight decrease of the average value of the gas to star mass ratio is observed in correspondence of the cluster centre, however also in this case no strong gradients have been found. We can therefore conclude that when observed in H I the Abell cluster 1367 almost completely disappears and the only evidence of its hidden presence is a slightly higher number of galaxies with a low gas to star mass ratio near the cluster core.

6.2 The H I mass distribution and optical luminosity function

The Abell 1367 local volume can be used for a more detailed analysis of selection effects representing a unique data set for which complete samples independently selected at optical and radio wavelengths are available. We are particularly interested in the comparison of the H I mass distribution and optical luminosity function (LF) estimated from the two samples. In the past, different authors have used optically selected samples to determine the H I mass distributions of galaxies in the local Universe obtaining results significantly different from radio-selected samples (Briggs & Rao 1993; Gavazzi et al. 2005; Springob et al. 2005a). We therefore used the optically selected sample extracted from SDSS-DR5, complete to $g < 17$ mag, in order to compare the H I distribution and the g-band LF for optically and H I selected galaxies.

Contrary to the H I selected sample, the SDSS sample is not complete in redshift, but the redshift completeness rapidly drops below 50 per cent for $g \sim 16.5$ mag ($\sim 3 \times 10^9\,\mathrm{L}_\odot$). This complicates the estimate of the LF at low luminosities. In order to overcome the redshift incompleteness of cluster samples, we used the *completeness-corrected* method proposed by De Propris et al. (2003). This method is based on the assumption that the spectroscopic sample (i.e. galaxies with redshift available) is 'representative' of the entire cluster, i.e. the fraction of galaxies that are cluster members is the same in the (incomplete) spectroscopic sample as in the (complete) photometric one.

[3] The majority of galaxies without redshift have a magnitude $g < 16.5$ mag, suggesting that a not negligible fraction is composed by background galaxies (Cortese et al. 2004).

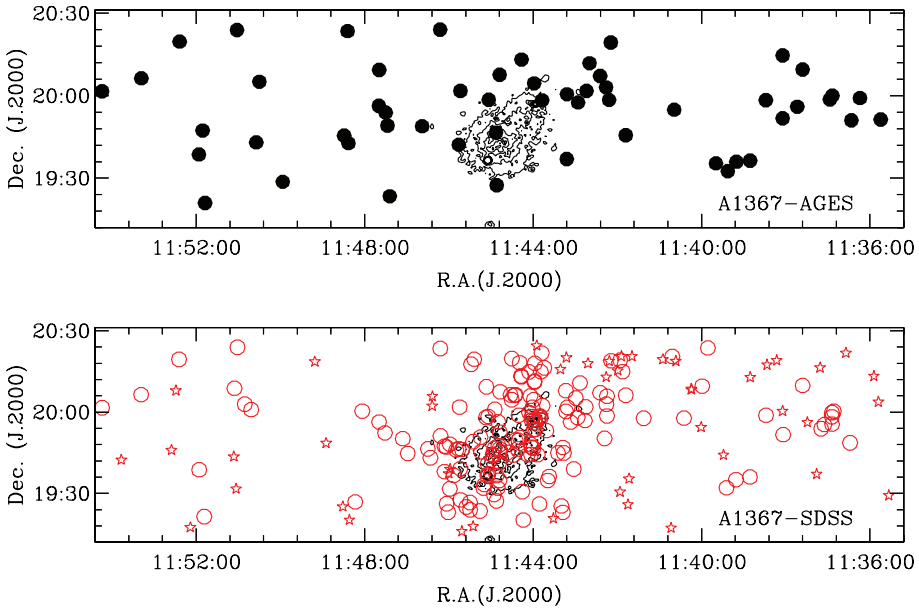

Figure 7. Upper panel: sky distribution of the members ($4000 < V < 10\,000\,\mathrm{km\,s^{-1}}$) of the Abell 1367 cluster in the H I selected sample. Lower panel: sky distribution of galaxies in the SDSS optically selected sample ($g < 17$ mag). Empty circles indicate confirmed cluster members and empty stars galaxies without redshift available. The black contours indicate the X-ray emission from A1367 as measured by *Roentgensatellit*.

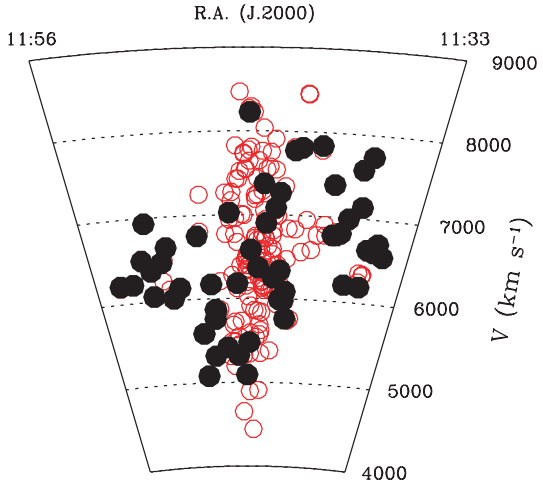

Figure 8. The wedge diagram of the AGES-A1367 region in the velocity range $4000 < V < 9000\,\mathrm{km\,s^{-1}}$. Filled circles indicate the H I detections while empty circles are galaxies belonging to the SDSS optically selected sample ($g<17$ mag).

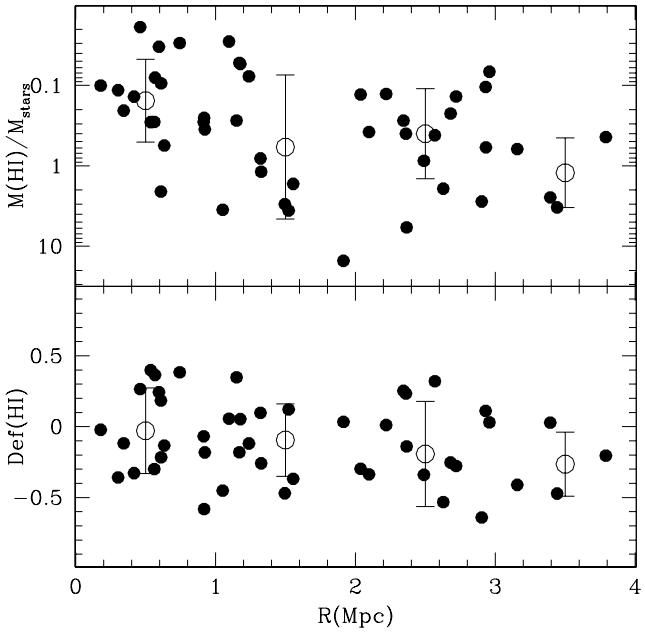

Figure 9. The distribution of the gas to star mass ratio (upper panel) and of the H I deficiency as a function of the projected distance from the centre of Abell 1367. Empty circles show the average values and standard deviations obtained in bins 1 Mpc wide.

The H I mass distributions obtained from the optically and H I selected samples are shown in Fig. 10. As expected, the two samples produce H I distributions significantly different. The optically selected sample drops quicker at low H I masses and does not include nearly half of the H I sources in the A1367 volume. The two samples start to differ at $M(\mathrm{H\,I}) \sim 2 \times 10^9\,\mathrm{M_\odot}$, well before our sensitivity limit. Low-luminosity, low surface brightness, gas-rich objects are in fact not included in the optical sample, but they represent a significant fraction of the total H I budget in Abell 1367. This result is consistent with the recent work by Springob et al. (2005a) who showed that the faint end slope of the H I mass function for an optically selected sample is less steep than the one obtained from a 21 cm selected sample. Our analysis suggests that this difference is mainly due to selection effects and that H I distributions obtained from optically selected samples cannot be generally considered as good proxies of the H I mass function in the local Universe.

The H I and optically selected samples also differ in the estimate of the optical LFs (Fig. 11, lower panel). The LF for the H I selected galaxies is flatter and includes fewer objects (i.e. lower Φ^*) than the one obtained from the optically selected sample. A great part of this difference is due to the overabundance of red ($g - i > 0.9$), gas-poor

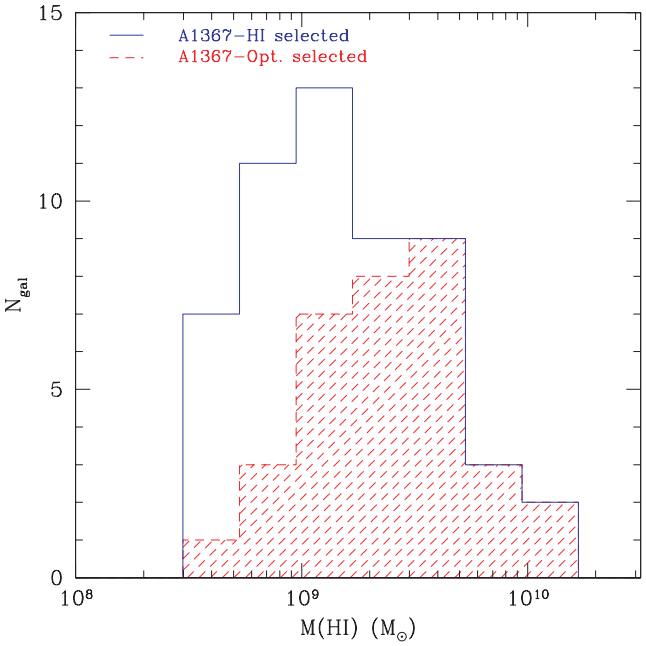

Figure 10. The H I mass distribution for galaxies in the A1367 volume. The solid histogram indicates the H I selected sample and the shaded histogram the optically selected sample extracted from SDSS-DR5 ($g < 17$ mag).

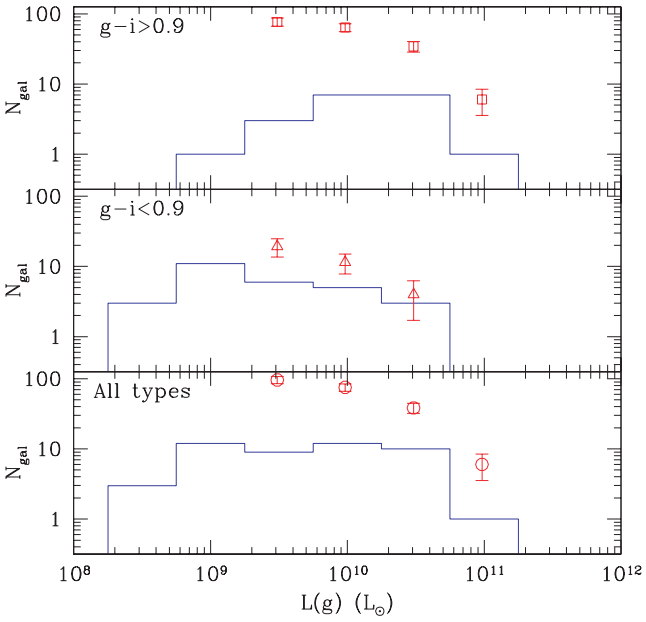

Figure 11. Each panel shows the g-band LF for galaxies in the A1367 volume as obtained from the optically (empty circles) and H I (histogram) selected sample. All galaxies in the two samples are shown in the bottom panel, while blue ($g - i < 0.9$) and red galaxies ($g - i > 0.9$) are shown in the middle and upper panel, respectively.

galaxies in the centre of Abell 1367: more than 80 per cent of bright red galaxies ($L > 10^9\,L_\odot$) in the A1367 region are not detected at 21 cm (see Fig. 11, upper panel). The difference between the two samples is less evident if we compare the LFs obtained only for blue galaxies (Fig. 11, middle panel), but even in this case the H I sample misses ∼30 per cent of blue cluster galaxies.

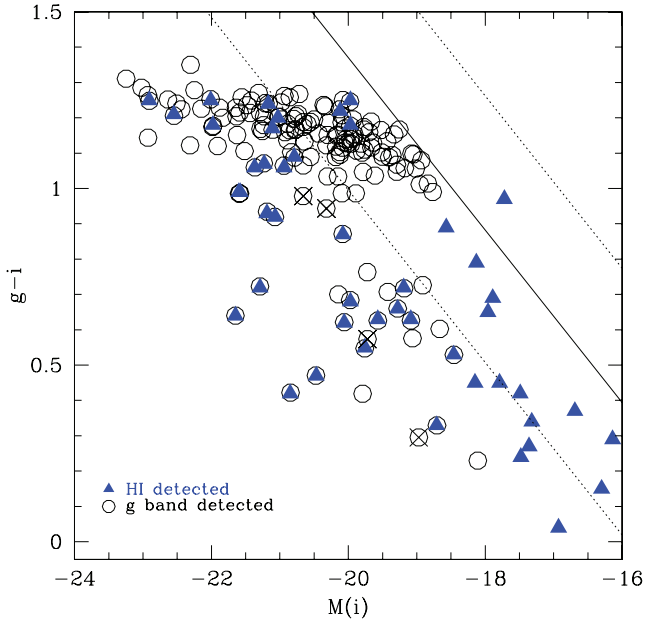

Figure 12. The $g - i$ colour $M(i)$ magnitude relation for confirmed cluster members in the Abell 1367 region. Triangles indicate galaxies detected in the AGES cube. Crosses indicate those galaxies lying in the RFIs velocity range or within the beam occupied by brighter sources. The solid (dashed) line indicates our sensitivity limit ($\pm 1\sigma$) obtained converting the H I sensitivity into colour limit using the $g - i$ versus $M(\mathrm{H\,I})/L(i)$ relation given by equation (6).

This result is quite interesting since we generally associate H I deficiency to red colours. In order to further investigate the properties of these blue galaxies not detected in H I, in Fig. 12 we compare the colour $g - i$, i magnitude relation for the confirmed cluster members in the optically (empty circles) and H I selected (triangles) samples. Almost all the H I galaxies lie on the blue sequence, but the opposite is not true: not all the galaxies in the blue sequence are detected in H I. This could be due to a number of different reasons. First of all, we have to take into account our sensitivity limit [$M(\mathrm{H\,I}) \sim 6 \times 10^8\,\mathrm{M}_\odot$ for $\mathrm{W}_{50} \sim 200\,\mathrm{km\,s^{-1}}$] which we need to relate to optical colour and magnitude. To do so, we have used the correlation between the H I mass and i-band luminosity ratio and the $g - i$ colour observed for our sample. The best bisector linear fitting gives the following relation:

$$g - i = (-0.61 \pm 0.05) \times \log\left[\frac{M(\mathrm{H\,I})}{L(i)}\right] + (0.57 \pm 0.04) \qquad (6)$$

with a dispersion of 0.37 dex. We can use this equation to estimate our sensitivity limit, which is indicated by the solid line in Fig. 12. We consider undetected blue galaxies those objects not detected by AGES, lying outside the 1σ region and with a $g - i$ colour bluer than 0.9 mag: 10 galaxies in total. Some of these sources lie within (in both space and velocity) strong H I galaxies and can be missed, due to the size of the Arecibo beam (FWHM ∼ 3.5 arcmin) and to the fact that in these cases the H I emission is totally assigned to the bright source. Moreover, some galaxies have a recessional velocity within the RFIs frequencies and cannot be detected. Excluding these cases (indicated with crosses in Fig. 12, left-hand side), we are left with eight blue galaxies which are not detected in H I. These objects have a g-band luminosity in the range $2 \times 10^9 < L_g < 10^{10}\,\mathrm{L}_\odot$ [i.e. $-19.4 < M(g) < -17.9$ mag], implying that we are dealing with intermediate-mass galaxies and not dwarf systems. Moreover,

Table 4. SDSS-blue galaxies undetected in H I.

RA (J2000)	Dec. (J2000)	Name	u (mag)	g (mag)	r (mag)	i (mag)	z (mag)	$g-i$ (mag)	V (km s^{-1})	$R_{\rm iso}(r)$ (arcsec)	$R_{\rm iso}$(H α) (arcsec)
11:42:18.12	+19:50:15.9	KUG 1139+201	17.15	15.88	15.40	15.12	14.98	0.76	6476	11.6	3.0
11:43:47.76	+20:21:48.0	KUG 1141+206A	17.59	16.12	15.66	15.43	15.25	0.71	6722	15.1	6.8
11:43:48.90	+20:14:54.0	KUG 1141+205	17.33	16.35	15.90	15.78	15.60	0.57	6103	8.0	4.8
11:43:49.88	+19:58:34.8	CGCG 97-087N	18.04	16.78	16.49	16.18	16.01	0.60	7542	19.0	6.0
11:43:58.23	+20:11:07.9	CGCG 97-092	16.46	15.39	14.95	14.70	14.52	0.70	6487	–	–
11:44:01.94	+19:47:03.9	CGCG 97-093	16.37	15.47	15.18	15.05	14.98	0.42	4909	24.0	9.1
11:44:13.90	+19:20:11.3	MAPS-NGP O_434_0047177	17.48	16.96	16.79	16.73	16.66	0.23	5852	10.3	8.6
11:44:54.56	+20:01:01.4	KUG 1142+202A	17.85	16.65	16.20	15.93	15.73	0.73	7646	10.8	3.2

their broad-band morphology and structural parameters are indistinguishable from the other blue H I detected galaxies. The limits obtained from equation (6) imply that the undetected galaxies have a H I deficiency $\geqslant$0.37, suggesting that we are dealing with blue, deficient objects, consistent with the marginal detection of two of these galaxies (CGCG97-092 and CGCG97-093) by deeper surveys (Gavazzi et al. 2006) implying a H I deficiency 0.31 and 0.57, respectively. This suggests that we are dealing with the same population of H I-poor, star-forming spirals originally observed in nearby clusters by Kennicutt, Bothun & Schommer (1984). Only when observed in Hα,[4] these galaxies appear different from healthy spirals, showing a truncation of the star-forming disc. In particular, in all but one object for which Hα data are available (eight galaxies; Iglesias-Páramo et al. 2002), the Hα radius (e.g. the isophotal radius within $10^{-16.5}$ erg cm^{-2} s^{-1} Å^{-1} arcsec^{-2}) is approximately two to four times less extended than the r-band 24th mag arcsec^{-2} isophotal radius (see Table 4). This is consistent with various independent studies (Catinella, Haynes & Giovanelli 2005; Boselli & Gavazzi 2006; Koopmann, Haynes & Catinella 2006) which have shown that the H I deficiency is associated with a truncation of the star-forming disc. All the deficient objects lie at a projected distance of less than $\sim$1° from the centre of Abell 1367, suggesting that the absence of H I and the truncation of the star formation disc are likely due to their interaction with the cluster environment. The fact that these objects have lost almost 40 per cent of their original gas content but their broad-band morphology and optical colours are still those typical of normal star-forming spirals implies that they are recent arrivals within the cluster environment. It appears that the neutral hydrogen has been already stripped well within the optical radius quenching the star formation in the galaxy outskirts, but A-type stars have not yet died and the galaxies still appear as blue as they were before losing their gas. Given that Hα traces stars younger than 2×10^7 yr and the typical lifetime of A stars is $\sim$1 Gyr, we can speculate that our galaxies started to lose their gas $\sim$100 Myr ago, in agreement with the typical time-scale for gas stripping observed in Virgo cluster galaxies (e.g. Vollmer et al. 2001, 2004; Boselli et al. 2006; Cortese et al. 2007) and predicted by numerical models (e.g. Abadi, Moore & Bower 1999; Shioya et al. 2002; Roediger & Brüggen 2007). In less than 1 Gyr, when all the A stars are dead, these objects will lie in the $g-i$ red sequence and will not be any different from the bulk of the gas-poor (red) galaxy cluster population. Only future detailed spectroscopic investigation will allow us the better estimate the time-scale of this transformation. Finally, it is interesting to note that this population of blue gas-poor galaxies corresponds to approximately one-third of the whole population of blue galaxies in the A1367-volume, supporting the idea that A1367 is a cluster still young, and a considerable number of objects are infalling into the cluster core for the first time (Cortese et al. 2004).

[4] The Hα emission of a galaxy is due to the hydrogen ionized in H II regions by massive ($> 10\,M_\odot$), young ($< 2 \times 10^7$ yr) stars.

7 SUMMARY AND CONCLUSIONS

We have presented the results of a H I blind survey of 5×1 deg^2 centred on the core of Abell 1367 as part of the AGES. 100 H I galaxies have been detected (79 new measurements and 50 new redshifts), half of which belong to the Abell 1367 volume. Comparing the properties of the H I selected galaxies with an optically selected sample extracted from SDSS-DR5, we have shown that the large-scale distribution of galaxies is strongly wavelength dependent: in H I, the cluster core almost completely disappears and H I selected galaxies are homogeneously distributed in the cluster volume. The difference between the two samples is even more evident when we compare their luminosity and H I distribution. Our optically selected sample misses a considerable number of low-luminosity, low surface brightness galaxies underestimating by almost a factor of 2 the number of H I-rich galaxies present in the cluster volume. On the contrary, our H I sample contains a factor of 3 less bright galaxies than the optical one. These are mainly ellipticals or early-type, red spirals, but also a not negligible fraction of the blue sequence cluster spirals is missed. All these blue gas-poor objects are located near the edge of the X-ray cluster contours suggesting that their gas has been recently ($\sim$100 Myr) stripped by ram pressure so that the galaxies are already gas poor whereas their stellar populations are still young.

Although the spatial and number distribution of samples selected at different wavelengths are significantly different, the internal properties of galaxies seem not to be significantly wavelength dependent. H I galaxies seem to follow the same scaling relations observed in optical and bigger galaxies are redder, have a higher surface brightness and lower gas content than lower luminosity galaxies. The most interesting result of our analysis is that the baryon fraction of our sample appears to be almost constant, suggesting the difference in the star to gas ratio observed between bright and faint galaxies is only due to a different star formation efficiency (i.e. the time-scale necessary to convert gas into stars). This is the first time that such a result is obtained from a H I selected sample and even if consistent with models of galaxy formation it suggests that during their evolutionary history less massive galaxies do not lose a larger fraction of their baryons than bigger objects.

The analysis presented in this paper points out the importance of H I blind surveys like AGES in order to have an unbiased view of the properties of galaxies in the local Universe. Once the survey is at a more advanced stage and the size of our sample is

significantly bigger than the one presented here, it will be possible to carry out more detailed quantitative studies and comparisons between optically and H I selected samples, gaining more insight into the evolutionary history of nearby galaxies.

ACKNOWLEDGMENTS

LC wishes to thank all the AGES consortium and in particular Elias Brinks and Noah Brosh for useful discussions and comments on this manuscript. LC is supported by the UK Particle Physics and Astronomy Research Council.

This work is based on observations collected at Arecibo Observatory. The Arecibo Observatory is part of the National Astronomy and Ionosphere Centre, which is operated by Cornell University under a cooperative agreement with the National Science Foundation. We wish to thank the Arecibo Observatory for granting us the time to complete this part of the project and its staff for the help during the observations and data reduction. The TAC of the Loiano telescope is acknowledged for the time allocation to this project. This research has made use of the NASA/IPAC Extragalactic Data base, which is operated by the Jet Propulsion Laboratory, California Institute of Technology, under contract to NASA and of the GOLDMine data base (Gavazzi et al. 2003).

Funding for the SDSS and SDSS-II has been provided by the Alfred P. Sloan Foundation, the Participating Institutions, the National Science Foundation, the US Department of Energy, the National Aeronautics and Space Administration, the Japanese Monbukagakusho, the Max-Planck Society and the Higher Education Funding Council for England. The SDSS web site is http://www.sdss.org/.

The SDSS is managed by the Astrophysical Research Consortium for the Participating Institutions. The Participating Institutions are the American Museum of Natural History, Astrophysical Institute Potsdam, University of Basel, University of Cambridge, Case Western Reserve University, University of Chicago, Drexel University, Fermilab, the Institute for Advanced Study, the Japan Participation Group, Johns Hopkins University, the Joint Institute for Nuclear Astrophysics, the Kavli Institute for Particle Astrophysics and Cosmology, the Korean Scientist Group, the Chinese Academy of Sciences (LAMOST), Los Alamos National Laboratory, the Max-Planck-Institute for Astronomy (MPIA), the Max-Planck-Institute for Astrophysics (MPA), New Mexico State University, Ohio State University, University of Pittsburgh, University of Portsmouth, Princeton University, the United States Naval Observatory and the University of Washington.

REFERENCES

Abadi M. G., Moore B., Bower R. G., 1999, MNRAS, 308, 947
Adelman-McCarthy J. K., Agüeros M. A., Allam S. S. et al., 2007, ApJS, 172, 634
Auld R., Minchin R. F., Davies J. I. et al., 2006, MNRAS, 371, 1617
Baldry I. K., Glazebrook K., Brinkmann J., Ivezic Z., Lupton R. H., Nichol R. C., Szalay A. S., 2004, ApJ, 600, 681
Barnes D. G. et al., 2001, MNRAS, 322, 486
Basilakos S., Plionis M., Kovač K., Voglis N., 2007, MNRAS, 378, 370
Bell E. F., McIntosh D. H., Katz N., Weinberg M. D., 2003a, ApJ, 585, L117
Bell E. F., McIntosh D. H., Katz N., Weinberg M. D., 2003b, ApJS, 149, 289
Boselli A., Gavazzi G., 2006, PASP, 118, 517
Boselli A., Lequeux J., Gavazzi G., 2002, A&A, 384, 33
Boselli A., Boissier S., Cortese L., Gil de Paz A., Seibert M., Madore B. F., Buat V., Martin D. C., 2006, ApJ, 651, 811
Briggs F. H., Rao S., 1993, ApJ, 417, 494
Buat V. et al., 2007, ApJS, in press (astro-ph/0609738)
Bullock J. S., Dekel A., Kolatt T. S., Kravtsov A. V., Klypin A. A., Porciani C., Primack J. R., 2001, ApJ, 555, 240
Catinella B., Haynes M. P., Giovanelli R., 2005, AJ, 130, 1037
Cayatte V., Kotanyi C., Balkowski C., van Gorkom J. H., 1994, AJ, 107, 1003
Chincarini G. L., Giovanelli R., Haynes M. P., 1983, ApJ, 269, 13
Cole S., Lacey C. G., Baugh C. M., Frenk C. S., 2000, MNRAS, 319, 168
Cortese L., Gavazzi G., Iglesias-Paramo J., Boselli A., Carrasco L., 2003, A&A, 401, 471
Cortese L., Gavazzi G., Boselli A., Iglesias-Paramo J., Carrasco L., 2004, A&A, 425, 429
Cortese L. et al., 2005, ApJ, 623, L17
Cortese L., Gavazzi G., Boselli A., Franzetti P., Kennicutt R. C., O'Neill K., Sakai S., 2006, A&A, 453, 847
Cortese L. et al., 2007, MNRAS, 376, 157
Cowie L. L., Songaila A., Hu E. M., Cohen J. G., 1996, AJ, 112, 839
Crain R. A., Eke V. R., Frenk C. S., Jenkins A., McCarthy I. G., Navarro J. F., Pearce F. R., 2007, MNRAS, 377, 41
Davies J. I., de Blok W. J. G., Smith R. M., Kambas A., Sabatini S., Linder S. M., Salehi-Reyhani S. A., 2001, MNRAS, 328, 1151
Davies J. et al., 2004, MNRAS, 349, 922
De Propris R. et al., 2003, MNRAS, 342, 725
Dressler A., 1980, ApJ, 236, 351
Freeman K. C., 1970, ApJ, 160, 811
Freudling W. et al., 2005, BAAS, 37, 1316
Gavazzi G., 1987, ApJ, 320, 96
Gavazzi G., 1989, ApJ, 346, 59
Gavazzi G., Pierini D., Boselli A., 1996, A&A, 312, 397
Gavazzi G., Franzetti P., Scodeggio M., Boselli A., Pierini D., 2000, A&A, 361, 863
Gavazzi G., Boselli A., Donati A., Franzetti P., Scodeggio M., 2003, A&A, 400, 451
Gavazzi G., Boselli A., van Driel W., O'Neil K., 2005, A&A, 429, 439
Gavazzi G., O'Neil K., Boselli A., van Driel W., 2006, A&A, 449, 929
Geha M., Blanton M. R., Masjedi M., West A. A., 2006, ApJ, 653, 240
Giovanelli R., Haynes M. P., 1985, ApJ, 292, 404
Giovanelli R., Haynes M. P., Herter T., Vogt N. P., Freudling W., Mala M. A. G., Salzer J. J., Wegner G., 1997, AJ, 113, 22
Giovanelli R. et al., 2005, AJ, 130, 2598
Giovanelli R. et al., 2007, AJ, 133, 2569
Girardi M., Giuricin G., Mardirossian F., Mezzetti M., Boschin W., 1998, ApJ, 505, 74
Governato F., Willman B., Mayer L., Brooks A., Stinson G., Valenzuela O., Wadsley J., Quinn T., 2007, MNRAS, 374, 1479
Haynes M. P., Giovanelli R., 1984, AJ, 89, 758
Haynes M. P., Giovanelli R., Herter T., Vogt N. P., Freudling W., Maia M. A. G., Salzer J. J., Wegner G., 1997, AJ, 113, 1197
Henning P. A. et al., 2000, AJ, 119, 2686
Henning P. A. et al., 2006, Bull. Am. Astro. Soc., 38, 133
Higdon S. J. U., Armus L., Higdon J. L., Soifer B. T., Spoon H. W. W., 2006, ApJ, 648, 323
Iglesias-Páramo J., Boselli A., Cortese L., Vílchez J. M., Gavazzi G., 2002, A&A, 384, 383
Kauffmann G. et al., 2003, MNRAS, 341, 33
Kennicutt R. C. Jr, Bothun G. D., Schommer R. A., 1984, AJ, 89, 1279
Koopmann R. A., Haynes M. P., Catinella B., 2006, AJ, 131, 716
Koribalski B. S. et al., 2004, AJ, 128, 16
Lang R. H. et al., 2003, MNRAS, 342, 738
Lewis B. M., 1983, AJ, 88, 962
McGaugh S., de Blok E., 1998, in Zaritsky D., ed., ASP Conf. Ser. Vol. 136, Galactic Haloes. Astron. Soc. Pac., San Francisco, p. 210
McGaugh S. S., Schombert J. M., Bothun G. D., de Blok W. J. G., 2000, ApJ, 533, L99
Meyer M. J., Zwaan M. A., Webster R. L., Brown M. J. I., Staveley-Smith L., 2007, ApJ, 654, 702
Minchin R. F. et al., 2003, MNRAS, 346, 787

Minchin R. F., Momjian E., Cortese L., O'Neil K. L., Henning P. A., Davies J. I., AGES Team, 2006, Bull. Am. Astro. Soc., 38, 1033
Minchin R. F. et al., 2007, in Combes F., Palous J., eds, IAU Symp., Vol. 235, p. 227
Roediger E., Brüggen M., 2007, MNRAS, 765
Rosenberg J. L., Schneider S. E., 2000, ApJS, 130, 177
Saintonge A., 2007, AJ, 133, 2087
Sakai S. et al., 2000, ApJ, 529, 698
Salpeter E. E., Hoffman G. L., 1996, ApJ, 465, 595
Sault R. J., Teuben P. J., Wright M. C. H., 1995, in Shaw R. A., Payne H. E., Hayes J. J. E., eds, ASP Conf. Ser. Vol. 77, Astronomical Data Analysis Software and Systems IV. Astron. Soc. Pac., San Francisco, p. 433
Shioya Y., Bekki K., Couch W. J., De Propris R., 2002, ApJ, 565, 223
Solanes J. M., Giovanelli R., Haynes M. P., 1996, ApJ, 461, 609
Solanes J. M., Manrique A., García-Gómez C., Gonzalez-Casado G., Giovanelli R., Haynes M. P., 2001, ApJ, 548, 97
Spitzak J. G., Schneider S. E., 1998, ApJS, 119, 159
Springob C. M., Haynes M. P., Giovanelli R., 2005a, ApJ, 621, 215
Springob C. M., Haynes M. P., Giovanelli R., Kent B. R., 2005b, ApJS, 160, 149
Sullivan, W. T. III, Bates B., Bothun G. D., Schommer R. A., 1981, AJ, 86, 919
Swaters R. A., van Albada T. S., van der Hulst J. M., Sancisi R., 2002, A&A, 390, 829
Tschöke D., Bomans D. J., Hensler G., Junkes N., 2001, A&A, 380, 40
Vollmer B., Cayatte V., Balkowski C., Duschl W. J., 2001, ApJ, 561, 708
Vollmer B., Balkowski C., Cayatte V., van Driel W., Huchtmeier W., 2004, A&A, 419, 35
Whitmore B. C., Gilmore D. M., Jones C., 1993, ApJ, 407, 489
Wong O. I. et al., 2006, MNRAS, 371, 1855
Zabludoff A. I., Geller M. J., Huchra J. P., Ramella M., 1993, AJ, 106, 1301

APPENDIX A: INTERESTING OBJECTS

High-velocity clouds. Two extended features well separated from the Milky Way emission and probably associated with HVCs have been detected in the velocity range $140 < V < 210\,\mathrm{km\,s^{-1}}$ (Fig. A1). The first lies in the range 11:50 < RA <11:55 and probably extends outside the region observed. The brightest region is in the south-east corner of the cube (11:54:00, +19:20:00, $160 < V < 210\,\mathrm{km\,s^{-1}}$) and a low column density stream seems to extend to the north-west. The second and strongest HVC occupies great part of the east part of the cube and extends over 1°.5 (11:40 < RA <11:46, 19:25 < Dec. <20:15) with a velocity in the range $140 < V < 175\,\mathrm{km\,s^{-1}}$.

CGCG97-027-group. The CGCG97-027-group is located at a projected distance of ∼2° (∼3.2 Mpc) from the centre of Abell 1367. It is composed of two star-forming spirals CGCG97-027 ($V \sim 6630\,\mathrm{km\,s^{-1}}$) and CGCG97-026 ($V \sim 6220\,\mathrm{km\,s^{-1}}$) and one lenticular CGCG97-023 ($V \sim 6320\,\mathrm{km\,s^{-1}}$). At a projected distance of ∼13 arcmin (∼0.7 Mpc) SW from the group lies the elliptical galaxy CGCG97-021 ($V \sim 6648\,\mathrm{km\,s^{-1}}$). Our data show the presence of diffuse H I emission all over the region occupied by the four bright Zwicky galaxies (see Fig. A2). In particular, high-velocity $6500 < V < 6800\,\mathrm{km\,s^{-1}}$ streams extend from CGCG97-021 to the north (Fig. A2, left-hand panel) and two of the H I sources without optical counterparts belong to this stream (AGES J113614+195910 and J113626+195102). Extended emission is also detected in the north part of the CGCG97-027 group in the velocity range $6000 < V < 6500\,\mathrm{km\,s^{-1}}$ (Fig. A2, right-hand panel).

CGCG97-041-group. The CGCG97-041-group is located at a projected distance of 1° (1.6 Mpc) from the centre of Abell 1367 and, as the CGCG97-027-group, it is composed of two spirals CGCG97-036 ($V \sim 6595\,\mathrm{km\,s^{-1}}$) and AGC210559 ($V \sim 6825\,\mathrm{km\,s^{-1}}$) and one lenticular CGCG97-041 ($V \sim 6778\,\mathrm{km\,s^{-1}}$). We detect H I emission extended over ∼200 kpc north of the three group members, apparently not associated with either of them (see Fig. A3).

AGES J113939+193524. This source ($V = 7382\,\mathrm{km\,s^{-1}}$) has no optical counterpart catalogued in the SDSS data base. However, in the SDSS plates a low surface brightness [$\mu(i) \sim 24\,\mathrm{mag\,arcsec^{-2}}$] galaxy is present in correspondence to the H I coordinates. We considered this object as candidate optical counterpart and labelled it as SDSSLSB in Table 3.

AGES J114239+201150. This source lies at a projected distance of ∼5.8 arcmin from the starburst galaxy CGCG97-068. No galaxies or extended features are found in deep CFHT *B* band (Gavazzi et al. 2003) and GALEX NUV–FUV (Cortese et al. 2005) data in correspondence with the peak of H I emission, suggesting that it could be a stream of gas stripped from CGCG97-068. Unfortunately, the distance of the source from CGCG97-068 is consistent with the region in which the first sidelobe is expected and the fact that AGES J114239+201150 lies at exactly the same recessional velocity of the starburst galaxy makes it impossible to discard the possibility that this source is sidelobe contaminated.

VLA D-configuration observations have been recently obtained for the interacting groups described above and for CGCG97-068, and will be used to study in detail the properties of these sources. The results of these observations will be presented in a forthcoming work.

(vi) AGES J114809+192109. This source ($V = 11\,252\,\mathrm{km\,s^{-1}}$) lies at the south edge of our cube and it is not clearly associated with any optical galaxy.

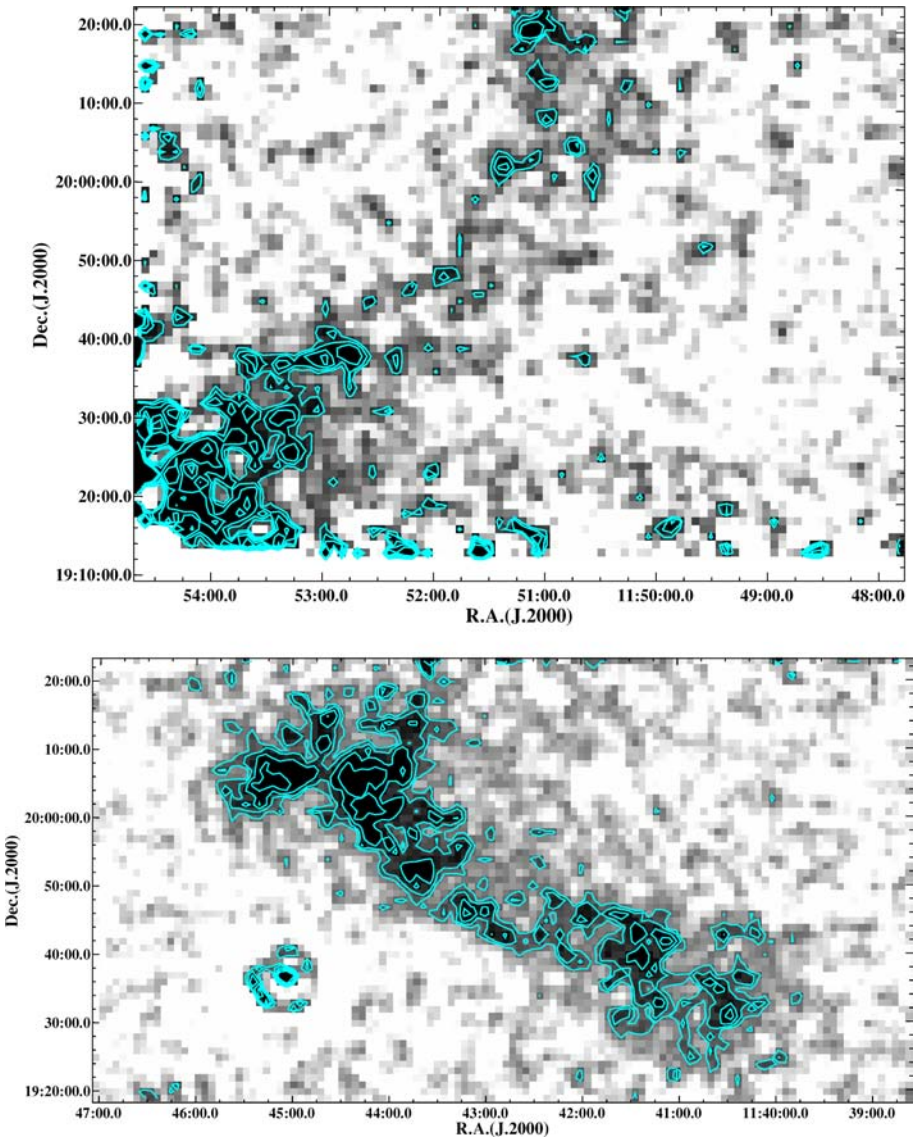

Figure A1. The two HVC complexes detected in the AGES-A1367 cube. The H I column density maps were obtained integrating the line emission in the data cube within the velocity range $160 < V < 210\,\mathrm{km\,s^{-1}}$ (left-hand panel) and $140 < V < 175\,\mathrm{km\,s^{-1}}$ (right-hand panel). Contours are superposed to the moment map: 0.08, 0.1, 0.12, 0.16 $\mathrm{Jy\,km\,s^{-1}\,beam^{-1}}$.

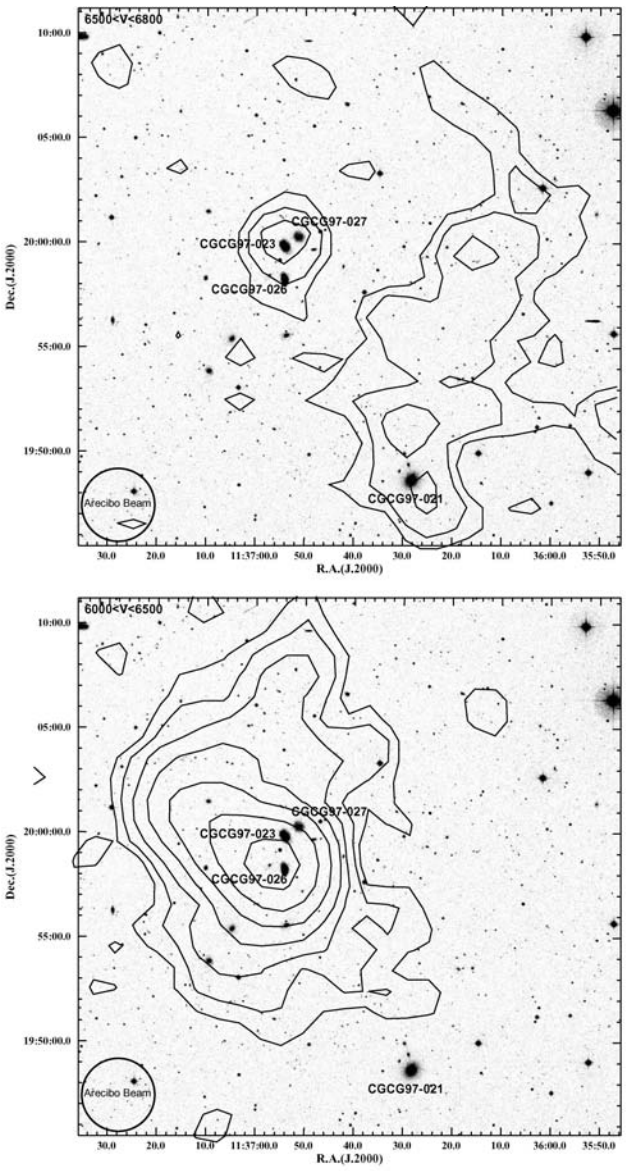

Figure A2. The CGCG97-027 group as seen on the Digital Sky Survey-blue plates. H I column density contours were obtained from moment maps of the AGES data cube in the velocity range $6500 < V < 6850\,\mathrm{km\,s^{-1}}$ (left-hand panel) and $6000 < V < 6500\,\mathrm{km\,s^{-1}}$ are superposed. Contour levels are as follows: 0.2, 0.3, 0.5 Jy km s^{-1} beam^{-1} (left-hand panel) and 0.3, 0.46, 0.71, 1.1, 1.7, 2.6, 4 Jy km s^{-1} beam^{-1} (right-hand panel).

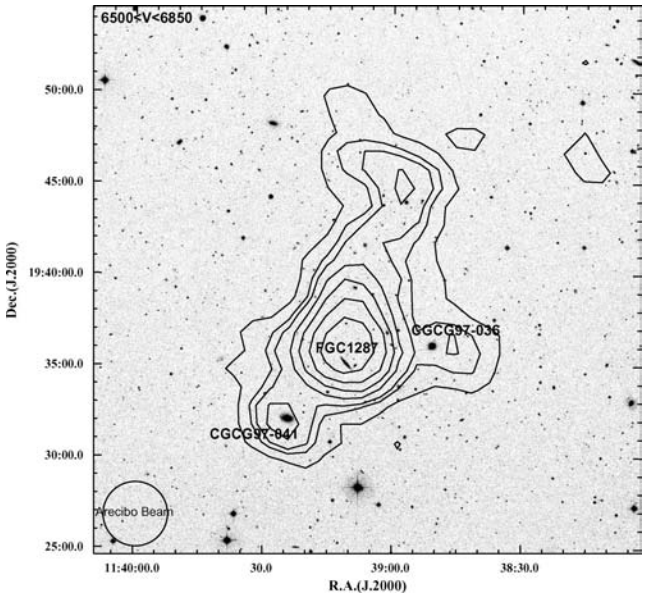

Figure A3. The CGCG97-041 group as seen on the DSS-blue plates. Radio contours obtained from moment maps of the AGES cube in the velocity range $6500 < V < 6850\,\mathrm{km\,s^{-1}}$. Contour levels are as follows: 0.18, 0.26, 0.36, 0.52, 0.73, 1.05, 1.5 Jy km s^{-1} beam^{-1}.

This paper has been typeset from a TEX/LATEX file prepared by the author.